2007

A study on buckled-beam actuators for RF MEMS applications

Seunghoon Park
Louisiana State University and Agricultural and Mechanical College

A STUDY ON BUCKLED-BEAM ACTUATORS FOR RF MEMS APPLICATIONS

A Thesis

Submitted to the Graduate Faculty of the
Louisiana State University and
Agricultural and Mechanical College
in partial fulfillment of the
requirements for the degree of
Master of Science in Electrical Engineering
in
The Department of Electrical & Computer Engineering

By
Seunghoon Park
B.S., Dong-A University, Korea, 2005
December 2007

ACKNOWLEDGEMENTS

The past two and a half years, working with Dr. Dooyoung Hah in the Optical & RF MEMS group in Louisiana State University was my greatest luck in my life. His countless suggestions and thoughtful guidance were much more than I could have ever imagined. Without his support, this thesis would not have been completed.

I am very thankful for my committee members, Drs. Pratul K. Ajmera, Martin Feldman, for their many invaluable suggestions and advices. I am also very grateful for Mr. Golden Hwaung, the EMDL manager, for many valuable advices for academic works and my life as well. I also really appreciate and won't forget the colleagues who shared the life in Baton Rouge. Lastly, I would like to express my endless love and thanks to my parents and sisters for their supports and encouragements.

TABLE OF CONTENTS

LIST OF TABLES

LIST OF FIGURES

ABSTRACT

When combined with MEMS actuators, a mechanical lock is a useful device for various applications including memory cells, micro-relays, micro-valves, optical switches, and digital micro-mirrors. It allows removal of actuation force during idle periods without affecting an actuated state of a device, which makes standing power consumption completely unnecessary. In this thesis, a bistable buckled-beam actuator for RF MEMS switch applications has been examined. The buckled-beam geometry was designed based upon theoretical analysis. It was fabricated by SU-8 lithography and copper pulse electroplating. It was actuated by the Lorentz force using external magnet and current flow through the beam. Measured switching currents (10 to 200 mA) agree well with theoretical values. Required actuation voltage was less than 0.4 V for 20 to 60 μm displacement.

The developed buckled-beams were incorporated into a RF MEMS switch design. The basic structure of the proposed switch is a combination of a coplanar waveguide and two buckled-beam actuators. The coplanar waveguide has a ground-signal-ground (GSG) configuration and its dimensions were designed for 50 Ω characteristic impedance over broad RF band. The proposed switch has several advantages compared to the conventional capacitive-type RF MEMS switches. First, since the electromagnetic actuation mechanism is adopted in the proposed switch, required actuation voltage is much lower than the electrostatic actuation mechanism. Second, all the structures can be made from the same layer so that only one mask is necessary for the entire process. Third, the trapped charge issue is dramatically diminished because

the actuators are separated from the coplanar waveguide, very low voltage is applied to the actuators, and the polarity of voltage on the actuators is continuously toggled.

The proposed RF MEMS switch finds a variety of usefulness in RF circuits and systems, including wireless communication devices – antenna switching, T/R (transmitter/receiver) switching, band selection, adjustable gain amplifiers; radar systems for military applications – phase shifters, phased array antennas; measurement equipments – impedance matching circuits, etc.

CHAPTER I. INTRODUCTION

1.1 RF MEMS switches

A micro-relay was one of the earliest research topics where MEMS (micro-electro-mechanical systems) technology has been applied to. The first MEMS micro-relay was reported in 1971 with an electrostatic-cantilever actuator gating low frequency signals [1.1]. Successful demonstration of MEMS micro-relays brought about shift of frequency of interest from low frequency to higher frequency (microwave and millimeter wave) where RF aspect has to be included in device design.

An RF switch finds a variety of usefulness in RF circuits and systems, including wireless communication devices – antenna switching, T/R (transmitter/receiver) switching, band selection, adjustable gain amplifiers; radar systems for military applications – phase shifters, phased array antennas; measurement equipments – impedance matching circuits, etc. For these areas, solid state switches have been widely used: GaAs FETs [1.2-1.4] and p-i-n diodes [1.5], but not without drawbacks. Capacitive coupling deteriorates signal isolation, especially beyond the X-band (7-12.5 GHz). Having nonlinear *I-V* characteristics, they suffer from severe nonlinearity; a typical third-order intercept point is 27-45 dBm [1.6].

It was mid-90s that RF MEMS switches were introduced. In some devices, physical contact between metal electrodes was made for RF signal to flow and removed to stop transmission [1.7-1.8]. In other devices, huge variation of capacitance value between a signal line and ground lines carried out switching [1.9-1.10]. RF MEMS

switches have several advantages over FETs and p-i-n diode switches. First, insertion loss, the decrease in transmitted signal power resulting from the insertion of a device, at an on-state is smaller over most of frequency range because of good ohmic contacts or low capacitive coupling. Both a p-n junction and a semiconductor channel have non-negligible resistance that causes significant insertion loss. Second, MEMS switches have very high linearity with third-order intercept point of 66-80 dBm [1.6] since they are essentially passive devices. This implies improved distortion characteristics [1.11]. Third, RF MEMS switches have significantly higher signal isolation at an off-state than their solid-state counterparts. Finally, MEMS switches can be fabricated on various kinds of substrates.

Like solid-state switches, RF MEMS switches can be divided into two categories depending on circuit configurations: a series type and a shunt type, as illustrated in Fig. 1.1. It is not always the case but in most of the cases, series-type switches incorporate metal-to-metal contacts [1.12], and shunt-type switches utilize capacitance changes [1.13].

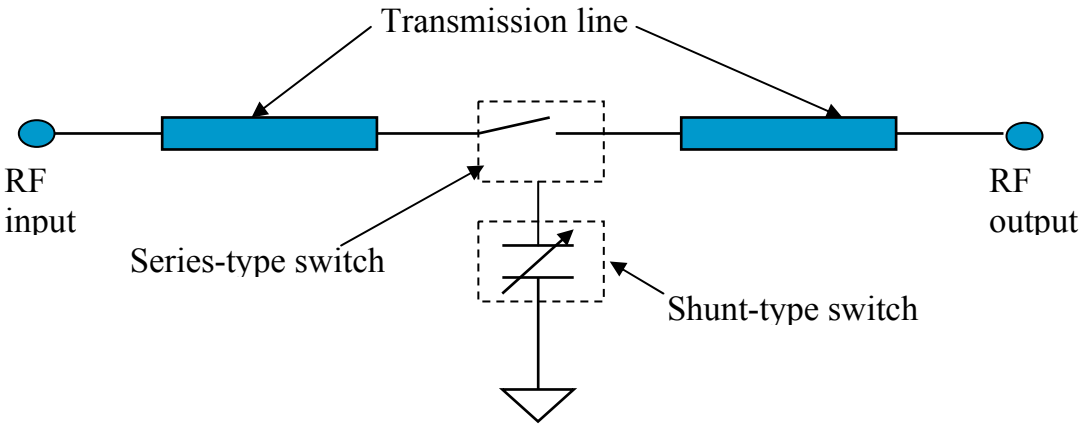

Figure 1.1. A schematic drawing of a series and a shunt-type switch.

Insertion loss and isolation are important figures of merit of RF MEMS switches. They are usually expressed by scattering (*S*) parameters. *S*-parameter matrix for a two-port network is illustrated in Fig. 1.2. Incident voltages at port 1 and 2 are denoted by a_1 and a_2, and voltages leaving port 1 and 2 are denoted by b_1 and b_2, respectively. Relationship of the voltages and S-parameters can be described as,

$$\begin{pmatrix} b_1 \\ b_2 \end{pmatrix} = \begin{pmatrix} S_{11} & S_{12} \\ S_{21} & S_{22} \end{pmatrix} \begin{pmatrix} a_1 \\ a_2 \end{pmatrix}.$$

Insertion loss at an on-state and isolation at an off-state are defined as following,

$$\textit{Insertion Loss} = 10 \log(|S_{11}|^2 + |S_{21}|^2)$$

$$\textit{Isolation} = 10 \log|S_{21}|^2.$$

1.1.1 RF MEMS switches with out-of-plane actuators

Depending on a moving direction with respect to a substrate, actuators can be generally divided into out-of-plane actuators and in-plane actuators. So far, most of the RF MEMS switches incorporated out-of-plane actuators.

An example of a metal-to-metal-contact switch (Rockwell Science Center) on a coplanar waveguide (CPW) is illustrated in Fig. 1.3. The signal line has a gap in the middle so that the output port is isolated from the input port. A suspended metal bar, anchored to a substrate through insulation layers, is situated above the signal line where the gap is. By applying high enough voltage between the suspended metal bar and ground electrodes, the metal bar is pulled down to make contacts with the signal line allowing signal transmission. When it is at an up state (Fig. 1.3(a)), DC resistance is infinite and capacitive coupling at high frequency is very small. When it is at a down

state (Fig. 1.3(b)), the signal line is connected with small contact resistance [1.13]. Insertion loss was lower than 0.2 dB, and isolation was better than 25 dB from DC to 40 GHz. Switching time was measured to be ~4 μs. Dimension of the switch part was 80 by 160 μm. Pull-down voltage was ~60 V. Lifetime of the switch was between 10^7 and 10^8 cycles.

Figure1.4 shows an example of a capacitive-shunt type MEMS switch (Raytheon). A CPW is made of 4-μm-thick aluminum [1.11]. A thin metal membrane is suspended on the signal line and attached to the ground lines. To prevent DC short between the metal membrane and the signal line, a dielectric layer (1000-2000 Å) is deposited on the signal line. Whole fabrication process is CMOS-process compatible. The membrane is electrostatically actuated by applying voltage between the bottom electrodes and the membrane. Between different membrane states (up and down), capacitance value (C_{off} and C_{on}) changes by a factor of 20-1000 [1.14]. Typically, capacitance in the membrane up state (C_{off}, or on state) is in the order of 35 fF between the membrane and the signal line, which induces small but not zero insertion loss. When the membrane is pulled down, the capacitance (C_{on}, or off state) is in the order of 21-35 pF creating low-impedance paths to the ground lines so that most of the signal is reflected at this huge impedance mismatch. A level of isolation at this state is determined by these capacitances. Dimensions of this switch were 120 by 280 μm. Pull-down voltage was ~50 V. Switching time was ~4 μs. Insertion loss and isolation at 35 GHz were 0.28 dB and -5 dB, respectively. Lifetime of the switch was 500 million cycles [1.15]. Since the ground lines and the signal line are connected through the membrane at off state, the

switch has a series inductance that makes the operation range narrow due to electrical resonance [1.16-1.17]. Its typical value is from 0.2 to 6 pH.

There are a number of other RF MEMS switches reported with some variations, but by and large, they are similar to those two examples just described. These RF MEMS switches with out-of-plane actuators have several drawbacks. Actuation voltage is usually high (typical, 15-80 V) because most of them use electrostatic actuators. Instead, electromagnetic actuators can be used, but they have an issue of high standing power consumption. They encounter failure at high RF power (>1 W). Capacitive-shunt type switches have narrowband isolation characteristics. For these reasons, in this thesis, laterally-driven bistable electromagnetic actuators in a buckled-beam shape have been studied for an RF MEMS switch application.

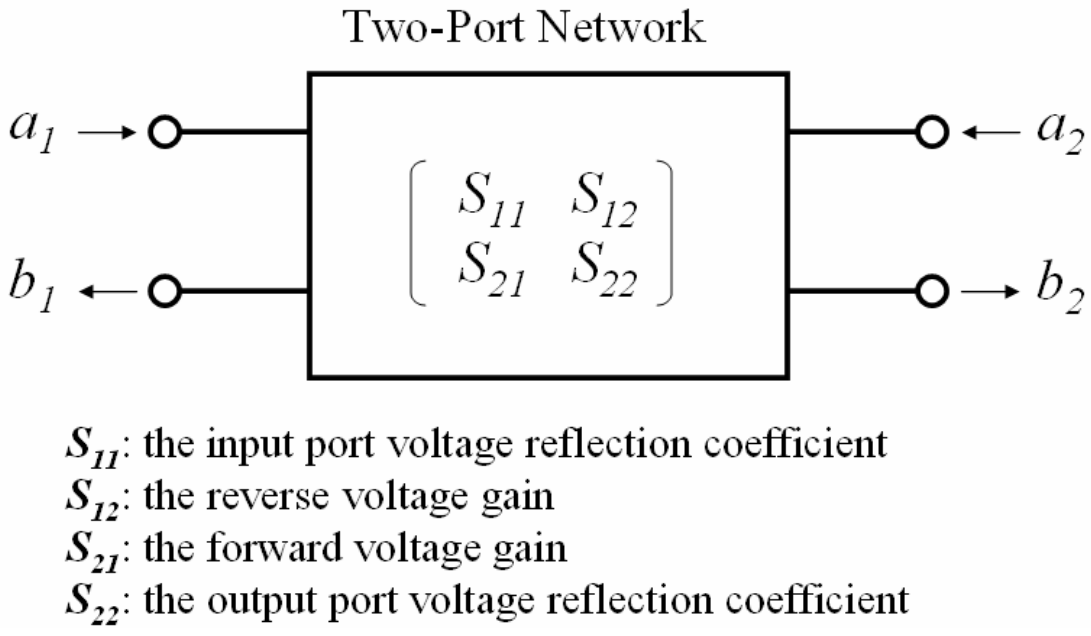

Figure 1.2. Scattering (*S*) parameters of a two-port network

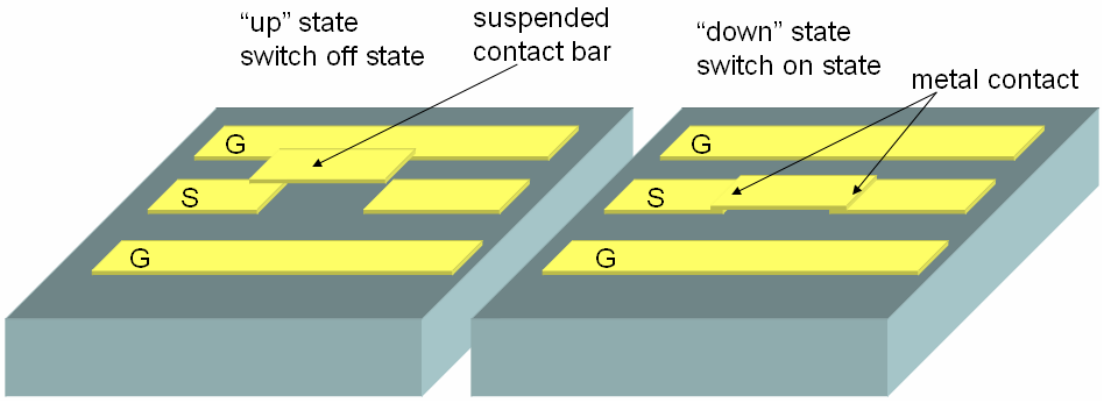

(a) (b)

Figure 1.3. A metal-to-metal-contact MEMS switch (a) at an off state ('up' or blocking state), and (b) at an on state ('down' or pass-through state) [1.12].

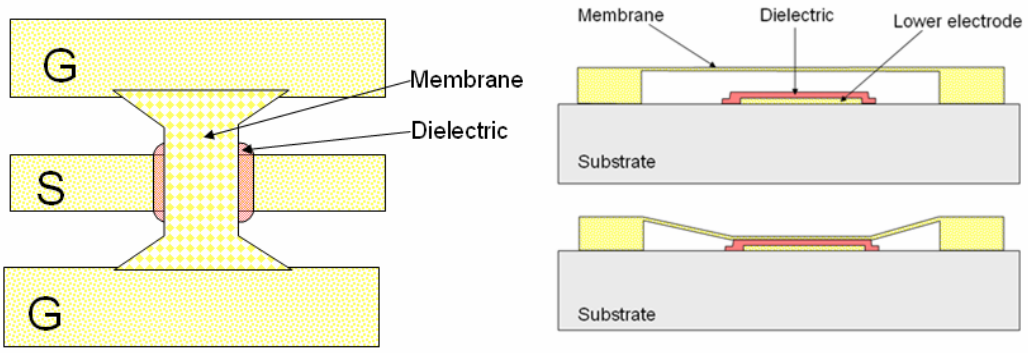

(a) (b)

Figure 1.4. Schematic drawings, (a) a top view of a capacitive-shunt type MEMS switch, and (b) cross sectional view of the switch at a non-actuated state (top, on state), and an actuated state (bottom, off state) [1.13].

1.1.2 RF MEMS switches with in-plane actuators

Min Tang et al. have reported a lateral series-type RF MEMS switch on a silicon-on-insulator (SOI) substrate based on a finite ground CPW configuration as shown in Fig. 1.5 [1.18, 1.19]. A signal line of the CPW has a gap in the middle. One part of the signal line has a cantilever structure that can be actuated electrostatically. The free end of the cantilever has a contact tip that faces another contact tip of the other part of the signal line. These two contact tips constitute a metal-to-metal contact-type switch. The cantilever is actuated by electrostatic potential difference between a fixed electrode and itself as shown in Fig. 1.6. When there is no potential difference (Fig. 1.6(a)), the switch is at an off state with high isolation. When the cantilever is actuated (Fig. 1.6(b)), contact is made with small contact resistance (switch on-state).

Measured isolation and insertion loss at 20 GHz were 16 dB and 1 dB, respectively. The operation voltage was 19.2 V, and the switching time was about 30 μs. This switch has an inevitable problem, i.e., due to the proposed configuration, feeding to the fixed electrode has to be located between a ground line and a signal line, which will significantly deteriorate its RF performance. In addition, an unusual shape of the signal line will make the RF performance even worse.

1.2 In-plane actuators

There are many applications where in-plane actuators can be more beneficial than out-of-plane actuators. In-plane actuators reported so far include electrostatic comb-drive actuators, U-shape electrothermal actuators, chevron-shape electrothermal actuators, and electromagnetic actuators utilizing the Lorentz force.

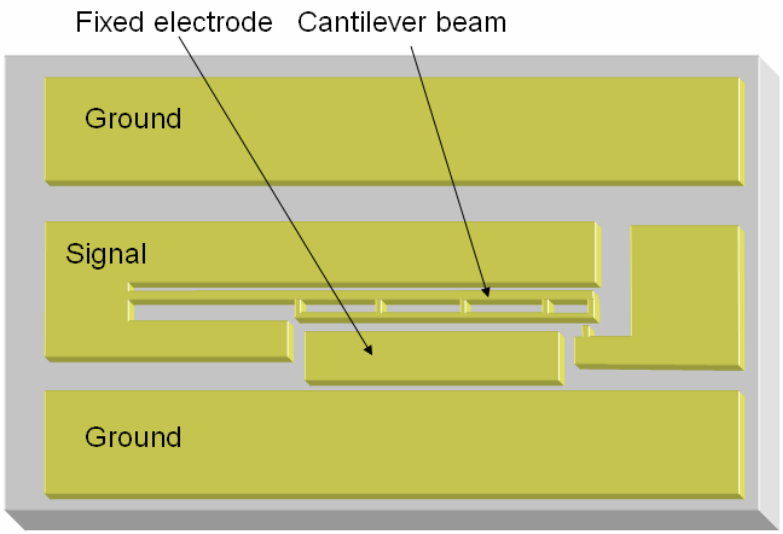

Figure 1.5. A schematic diagram of a lateral series switch [1.18].

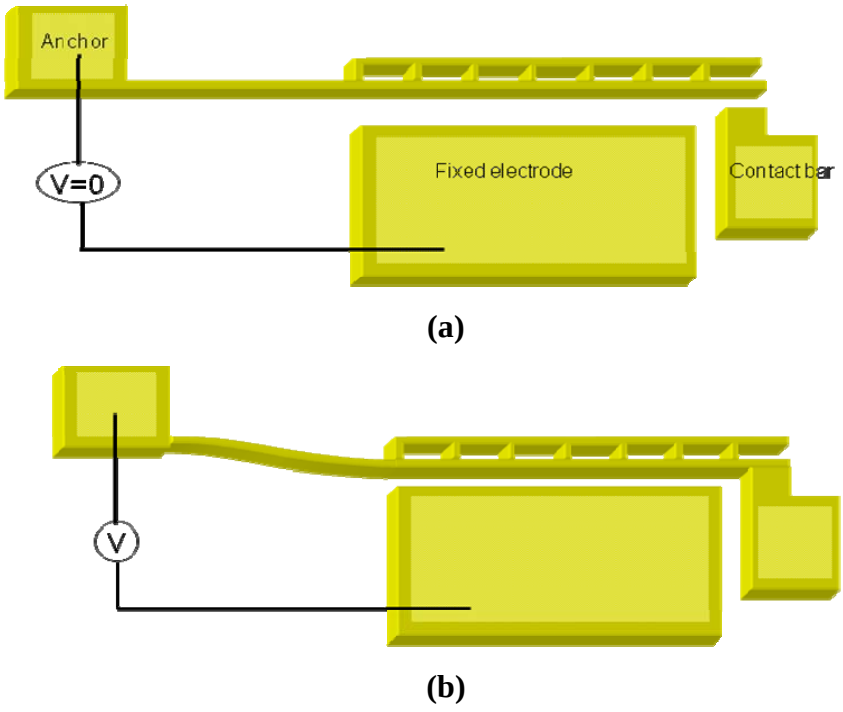

Figure 1.6. Schematic diagrams of the switch actuation. (a) Switch off-state (no voltage applied between the fixed electrode and the cantilever), and (b) switch on-state (voltage applied).

Table 1.1 Comparison of actuators

	Electrostatic	Electro-thermal	Electro-magnetic	Electromagnetic w/ bistability
Power Consumption	low	high	high	low
Force	small	high	high	high
Speed	fast	slow	fast	fast
Deflection	small	large	large	large
Driving type	voltage	current	current	current

1.2.1 Electrostatic comb-drive actuators

A comb drive actuator consists of interdigitated electrodes as illustrated in Fig. 1.7. As electric potential presents between one of fixed combs and a moving comb, the moving comb is attracted towards the fixed comb. One of the advantages of the comb drive actuator is low power consumption. One of its drawbacks is that it requires high voltages. Not to employ additional high voltage drive chips, actuation voltage should drop at least below 5 V to be compatible with CMOS circuits. This could be achieved by narrowing gaps between comb fingers, increasing finger heights, or increasing a number of fingers, but with technical difficulty. Narrowing gaps increases risk of mechanical movement failures, namely, lateral instability.

1.2.2 Electrothermal actuators

Electrostatic actuators require high actuation voltages and exert low force. On the other hand, electrothermal actuators require high actuation current and are able to drive with high force for large displacement. Two types of electrothermal actuators – a U-shape actuator (Fig. 1.8(a)) [1.20] and a chevron-shape actuator (Fig. 1.8(b)) [1.21] –

have been studied so far. Voltage and current ranges of these actuators are generally compatible with CMOS circuits. However, they consume high power and their speeds are relatively slow.

1.2.3 Electromagnatic actuators

Several types of electromagnetic actuators have been introduced, such as variable reactance actuators [1.22] and Lorentz force actuators [1.23-1.24]. A fabrication process of the former one is rather complicated. Conversely, the latter one (Fig. 1.9) can be fabricated by simple process steps. A performance comparison table as summarized in table I shows that an electromagnetic actuator outperform other actuators. It is capable of high force drive, large deflection, low voltage operation, and fast speed. Like electrothermal actuators, its major drawback is high power consumption. By incorporating a bistability feature by modifying an actuator shape, this issue can be addressed as presented in chapter II.

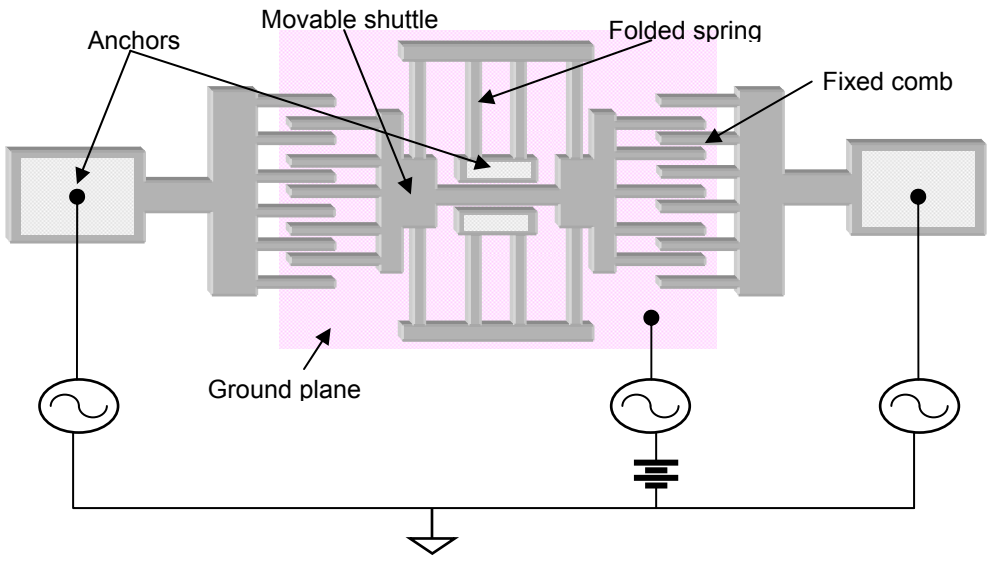

Figure 1.7. Schematic drawing of a combdrive actuator.

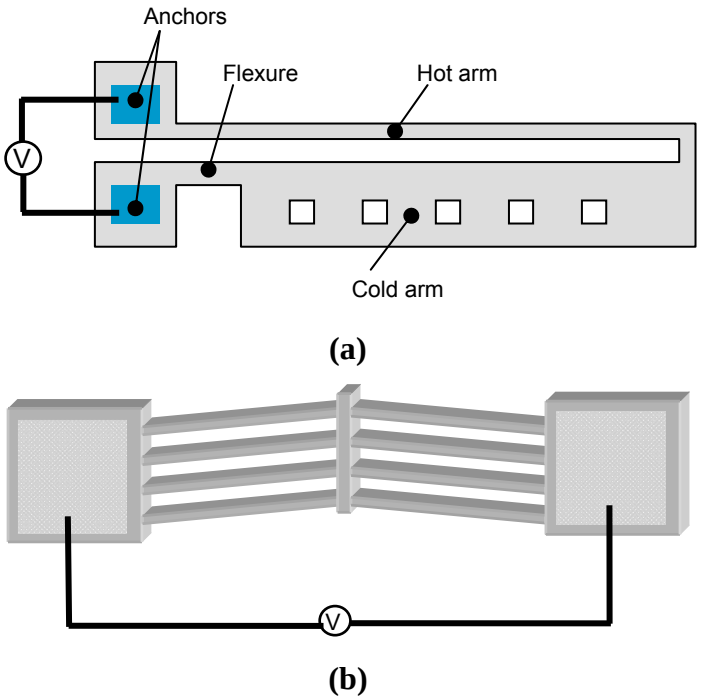

Figure 1.8. Sketches of (a) a U-shape (one hot arm) electrothermal actuator, and (b) a chevron-shape electrothermal actuator.

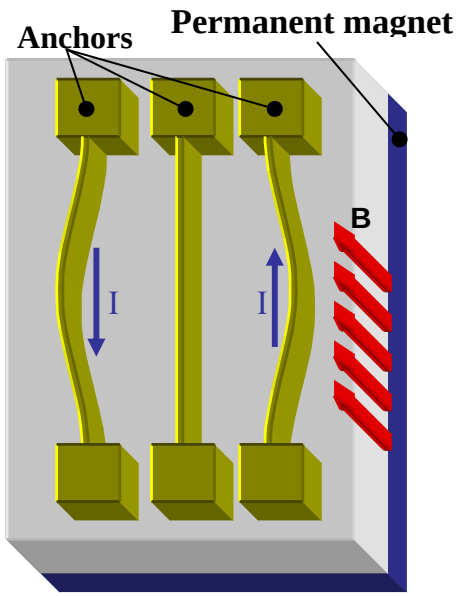

Figure 1.9. A sketch of an electromagnetic actuator with a permanent magnet attached at the bottom of a substrate.

CHAPTER II. BUCKLED-BEAM ACTUATORS

2.1 Introduction

When combined with MEMS actuators, a mechanical lock is a useful device for various applications including memory cells, micro-relays, micro-valves, optical switches, and digital micro-mirrors. It allows removal of actuation force during idle periods without affecting an actuated state of a device, which makes standing power consumption completely unnecessary. There have been several different kinds of locking mechanisms proposed by a number of groups. Hoffman et al. used a movable V-grooved clamp to lock an optical fiber for a 1×2 optical switch application [2.1]. Jensen et al. introduced the design optimization of the hinged multi-segment mechanisms [2.2]. Liu et al. implemented locking by engaging teeth between locking actuators and a driving actuator [2.3]. There are locking methods other than using mechanical locks. Texas Instruments' digital micromirror devices (DMD) utilize hysteresis in an electrostatic actuator to obtain bistability [2.4].

With its bistability characteristic, a buckled beam is particularly interesting for its simple structure. There are generally two methods to produce a buckled beam. One is to pattern a beam in a buckled shape [2.5] and the other is to fabricate a straight beam first and then make them buckled afterwards by applying compressive stress [2.6]. For the latter, compressive stress can be applied either by additional actuators or by residual stress of a bimorph. Generation of a buckled-beam shape from a layout stage is

advantageous in that it does not require auxiliary actuators, needs just a small footprint, and can have a well-controlled geometry.

In this study, a buckled-beam actuator has been examined. Its buckled geometry was defined by layout based upon theoretical analysis. It was fabricated by SU-8 lithography and copper pulse electroplating. It was actuated by the Lorentz force using external magnet and current flow through itself. Required actuation voltage is much lower than that of electrostatic or piezoelectric actuators.

2.2 Theoretical analysis

To design the buckled-beam actuator, theoretical analysis has been performed. The model which the beam analysis is based upon is similar to the one provided by Qiu et al. in [2.**7**] although the loading conditions are different.

Figure 2.1 is a sketch of a buckled-beam. The dimensions of the beam (width w, thickness t, length l) and the initial rise h are the important design parameters. The governing beam equation describing the relationship between its displacement v and axial load P is

$$EI\frac{d^4v}{dx^4}+P\frac{d^2v}{dx^2}=0 \tag{2.1}$$

where E and I are the Young's modulus of the beam material and the moment of inertia of the beam, respectively. With clamped-clamped-beam boundary conditions ($v(0)$ = $v(l)$ = 0, $dv/dx|_{x=0}$ = $dv/dx|_{x=l}$ = 0), nontrivial solutions for the beam displacement have the following form.

$$v(x)=v_0(x)-\sum_{n=1}^{\infty}a_n\sin^2\left(\frac{n\pi x}{l}\right) \tag{2.2}$$

where $v_0(x)$ represents the as-fabricated beam shape and a_n is the amplitude of n^{th} sinusoidal component of the beam displacement, whose spatial frequency is $n/2l$. If $v_0(x)$ is given as

$$v_0(x) = h\sin^2\left(\frac{\pi x}{l}\right) \tag{2.3}$$

and a uniform load q is applied in y-direction, high-order components are suppressed so that the beam displacement can be simplified as

$$v(x) = v_0(x) - a_1\sin^2\left(\frac{\pi x}{l}\right) = v_0(x) - \frac{a_1}{2}\left(1-\cos\frac{2\pi x}{l}\right). \tag{2.4}$$

Considering an axial load P and a bending moment M, the strain energy U stored in the buckled-beam when a uniform load q is applied can be expressed as

$$U = \int_0^l \left[\frac{\{P(x)\}^2}{2EA} + \frac{\{M(x)\}^2}{2EI} + q\{v(x) - v_0(x)\}\right]dx \tag{2.5}$$

where

$$P(x) = EA\varepsilon(x) = EA\frac{\sqrt{(dx)^2 + \left(dx\frac{dv}{dx}\right)^2} - \sqrt{(dx)^2 + \left(dx\frac{dv_0}{dx}\right)^2}}{\sqrt{(dx)^2 + \left(dx\frac{dv_0}{dx}\right)^2}} \tag{2.6}$$

$$= \frac{EA}{2}\left\{\left(\frac{dv}{dx}\right)^2 - \left(\frac{dv_0}{dx}\right)\right\} = \frac{EA\pi^2(a_1 - 2a_1h)}{4l^2}\left\{1-\cos\left(\frac{4\pi x}{l}\right)\right\}$$

And

$$M(x) = -EI\left(\frac{d^2v}{dx^2} - \frac{d^2v_0}{dx^2}\right) = EI\frac{2\pi^2 a_1}{l^2}\cos\left(\frac{2\pi x}{l}\right) \tag{2.7}$$

where $\varepsilon(x)$ represents the strain. Replacing $P(x)$ and $M(x)$ in (2.5) results in,

$$U = \frac{3EA\pi^4\left(a_1^4 - 4ha_1^3 + 4h^2a_1^2\right)}{64l^3} + \frac{\pi^4 a_1^2 EI}{l^3} - q\frac{a_1 l}{2}. \tag{2.8}$$

The load (q) versus amplitude (a_1) relationship can be found from (2.8), by using the fact that the amplitude should minimize the strain energy. Hence,

$$\begin{aligned} \frac{\partial U}{\partial a_1} &= \frac{3EA\pi^4\left(a_1^3 - 3ha_1^2 + 2h^2a_1\right)}{16l^3} + \frac{2\pi^4 a_1 EI}{l^3} - q\frac{l}{2} = 0 \\ q &= \frac{3EA\pi^4\left(a_1^3 - 3ha_1^2 + 2h^2a_1\right)}{8l^4} + \frac{4\pi^4 a_1 EI}{l^4}. \end{aligned} \tag{2.9}$$

Figure 2.2, the plot of q versus a_1, indicates that the amplitude is proportional to the load for small loading. When the load reaches a certain value, the amplitude hits a local maximum. This displacement is called as the critical displacement. Beyond the critical displacement, the graph shows a negative slope, which is physically unreal. What really should happen is, when the applied load is beyond the critical load, the buckled-beam abruptly moves from point A to point B. When the load is withdrawn after this occurs, the beam doesn't come back to the original position (O_1) but rests at the second stable position (O_2). To move the beam back to its original position (O_1), the load has to be applied in the opposite direction and another critical amplitude has to be passed. When these conditions are met, the buckled-beam will abruptly move from point C to point D, and if the load is withdrawn after this, the beam rests at O_1. The first critical amplitude is called as the forward critical amplitude a_{crf} and the second one as the backward critical amplitude a_{crb}.

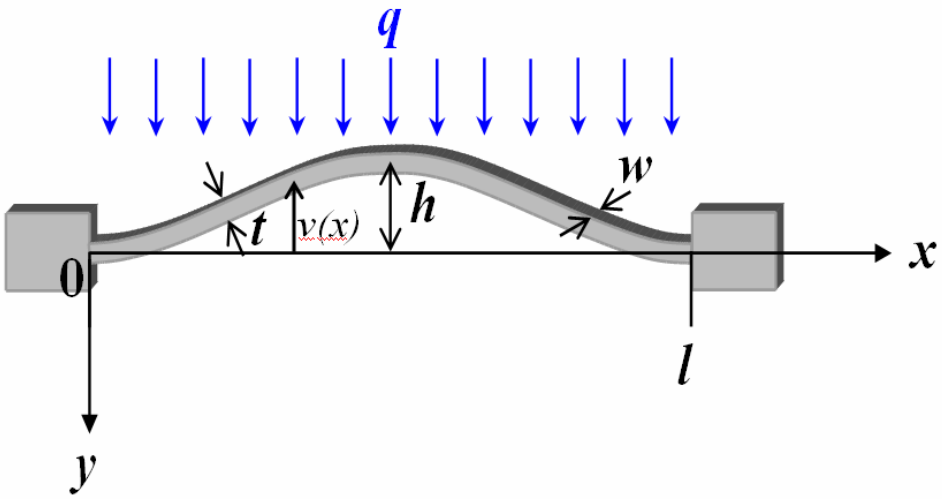

Figure 2.1. A sketch of a buckled-beam.

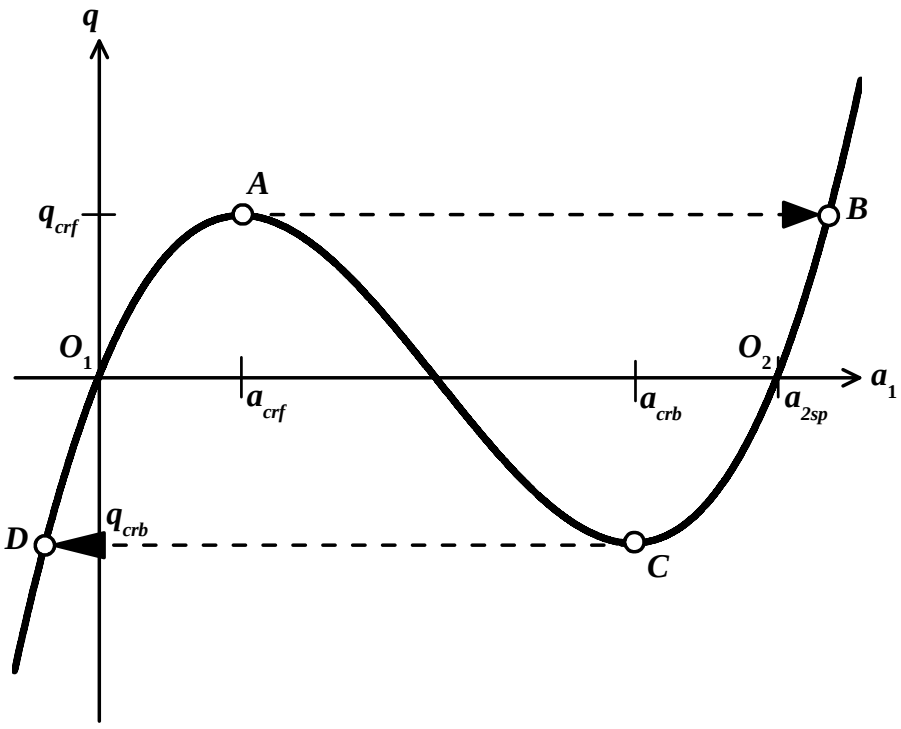

Figure 2.2. Applied load (q) versus displacement amplitude (a_1).

In the same way, two critical loads are named as the forward critical load q_{crf} and the backward critical load q_{crb}. The critical amplitudes and the critical loads can be found where the slope of the curve is zero;

$$\frac{\partial q}{\partial a_1} = \frac{3EA\pi^4\left(3a_1^2 - 6ha_1 + 2h^2\right)}{8l^4} + \frac{4\pi^4 EI}{l^4} = 0$$

$$a_1\big|_{\partial q/\partial a_1 = 0} = h \pm \sqrt{\frac{h^2}{3} - \frac{8t^2}{27}} \tag{2.10}$$

$$\therefore a_{crf} = h - \sqrt{\frac{h^2}{3} - \frac{8t^2}{27}} \quad \text{and} \quad a_{crb} = h + \sqrt{\frac{h^2}{3} - \frac{8t^2}{27}} \ .$$

The forward and backward critical loads are

$$q_{crf} = \frac{\pi^4 EI}{l^4}\left\{\frac{9}{t^2}\left(\frac{h^2}{3} - \frac{8t^2}{27}\right)^{\frac{3}{2}} + 4h\right\} \text{ and } q_{crb} = \frac{\pi^4 EI}{l^4}\left\{-\frac{9}{t^2}\left(\frac{h^2}{3} - \frac{8t^2}{27}\right)^{\frac{3}{2}} + 4h\right\}. \tag{2.11}$$

One interesting fact from (2.10) is that two critical amplitudes are symmetric against the x-axis (Fig. 2.1). According to (2.11), the forward critical load is larger than the backward critical load. The second stable position (a_{2sp}) can be found as the greatest solution for an equation of $q = 0$;

$$a_{2sp} = \frac{3}{2}h + \sqrt{\frac{h^2}{4} - \frac{8t^2}{9}} \ . \tag{2.12}$$

In order for a buckled-beam to have a second stable position, i.e. bistability, the term inside the square-root of (2.12) must be a positive value. When it is zero, the second stable position becomes equal to the backward critical amplitude, and when it is a negative value, the second stable position no longer exists. So the condition for the buckled-beam to have the bistable characteristic is,

$$h > \frac{4\sqrt{2}}{3} t . \quad (2.13)$$

2.3 Design

Based on the theoretical analysis described in the section 2.2, design of buckled-beam was performed. To compare the experimental observation with the theory, buckled-beams with 60 different geometries were included in the layout design: length (l) ─ 1500, 2000, 2500, and 3000 μm; thickness (t) ─ 5, 10, and 15 μm; width (w) ─10 μm; initial rise (h) ─ 10, 15, 20, 25, and 30 μm. The coordinates of the vertices of the beams were calculated using a spreadsheet software, and then imported to a layout tool, L-Edit in the CIF format. Figure 2.3 shows an image of the designed buckled-beams captured from the L-Edit software. Two squares in the middle of each beam, are included to measure the approximate position of the second stable point (O_2 in Fig. 2.2), and are 100 μm apart from each other. The size of the contact pads is 150 × 150 μm^2.

2.4 Fabrication

The designed fabrication process flow is depicted in Fig. 2.4. The fabrication sequence is seed layer deposition, SU-8 lithography, copper electroplating, SU-8 removal, seed layer strip, and release by substrate under-etch.

2.4.1 Wafer Preparation

Buckled-beams were fabricated on a 4" Borofloat glass wafer (thickness: 700 μm). The Borofloat glass wafer was selected for its fast etch rate in hydrofluoric (HF) acid: ~7 μm/min in 49 % HF. First, the glass wafer was cleaned in the piranha solution for one hour to get rid of organic materials. Piranha solution is a 1:1 mixture of

concentrated 30% hydrogen peroxide (H_2O_2) and 98 % concentrated sulfuric acid (H_2SO_4). The wafer was rinsed with DI water and dehydrated on a hot plate for 10 min at 200 °C.

2.4.2 Seed Layer Deposition

For the later electroplating process, a seed metal layer needs to be coated prior to the lithography step. For this purpose, Ti (20 nm)/Cu (30 nm) was deposited using the thermal evaporator at the EMDL. Titanium acts as an adhesion promotion layer between the copper layer and the glass substrate. The deposition rates of Ti and Cu were 0.5 and 2 nm/sec, respectively.

2.4.3 SU-8 Photolithography

SU-8 resist was used to form electroplating molds. SU-8 was selected for its excellent characteristic, i.e. high-aspect-ratio structures with almost vertical sidewalls. SU-8 2010 was spin-coated on the glass wafer as its spin coating parameters are depicted in Fig. 2.5. According to the manufacturer's datasheet, the expected thickness of the resist was 13 μm, but in reality, 10 μm-thick resist was achieved.

After spin-coating, edge beads were removed by gently scraping the edge of the wafer (~1 mm from the edge) with micro slides (Fig. 2.6). Then, the wafer was put on a leveled table for 10 minutes to reduce surface roughness in the SU-8 layer. Next, the SU-8 layer was soft-baked on a hot plate according to a thermal cycle shown in Fig. 2.7.

After cooled down to a room temperature, the wafer was exposed to UV with the energy density of 120 mJ/cm^2. This exposure dose was decided based on the datasheet provided by the manufacturer, MicroChem Corp. (Fig. 2.8). The dose was multiplied by

1.5 considering that the substrate was coated with copper as recommended by the manufacturer [2.5]. The UV intensity of the Quintel aligner in the EMDL was measured as shown in table 2.1 to determine the exposure time. The appropriate exposure time was calculated to be 40 seconds.

Table. 2.1. UV intensity of the Quintel aligner

Wave Length	w/o filter	w/ filter
300 nm	2.6	0.1
365 nm	5.8	4.7
405 nm	12.1	10.3
436 nm	13.0	11.0

Absorption spectra of SU-8 resist for various thicknesses are shown in the Fig. 2.9. Absorption unit (AU) is a logarithmic unit used to measure optical density, the absorbance of light transmitted through a partially absorbing substance. If the absorbance is 1.0 AU, then 10% UV light is transmitted. An increase in absorbance of 1.0 AU corresponds to a reduction in transmittance by a factor of 10. Most of the light whose wavelengths are shorter than 360 nm is absorbed near the surface of the SU-8 layer. Therefore, it produces a cross-section with broader top and narrower base; so-called a T–topping problem. To overcome this problem, a filter (PL-360-LP from Omega Optical) was used to cut off the wavelength below 360 nm. Its transmission at 365, 405, and 436 nm mercury lines is better than 90% [2.9]. When the filter was not

used, patterns with narrow spacing (<5 μm) were not developed due to swelling of the surface areas.

After exposure, post-exposure-bake was performed. Its thermal cycle is the same as that of soft-bake (Fig. 2.7). Then, the SU-8 was developed in an SU-8 developer for 3 minutes with agitation. The substrate was rinsed with IPA for 2 minutes and dried with a nitrogen blower.

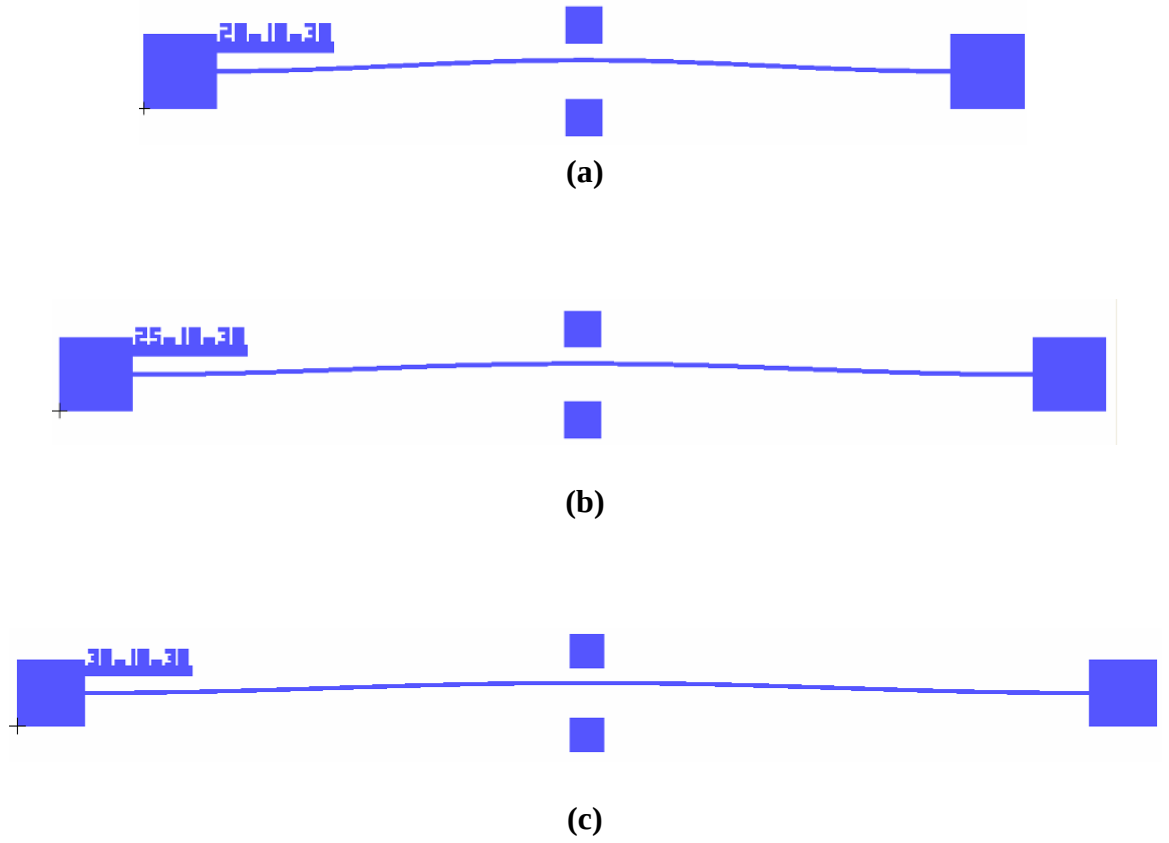

(a)

(b)

(c)

Figure 2.3. Images of the designed buckled-beams captured from the L-Edit, whose dimensions (l, t, h) are: (a) 2000, 10, 30 μm, (b) 2500, 10, 30 μm, and (c) 3000, 10, 30 μm.

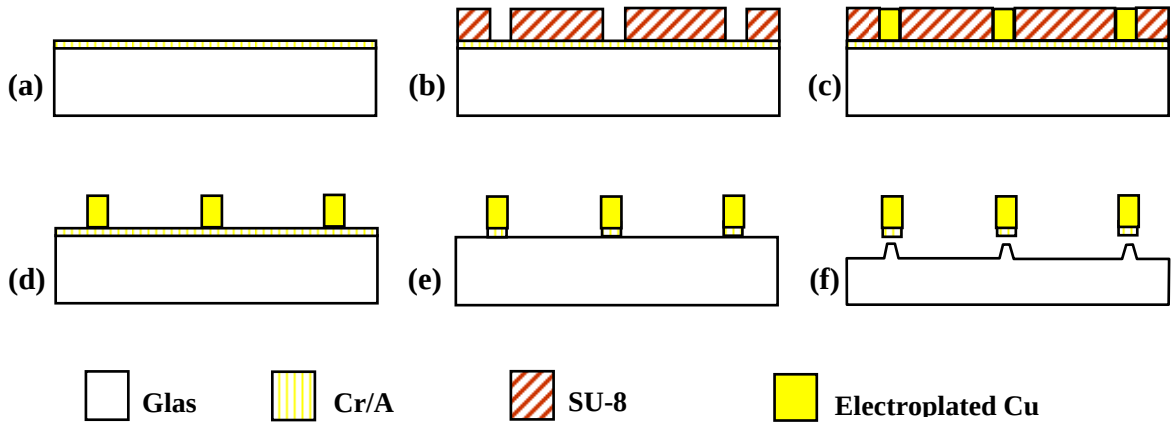

Figure 2.4. Fabrication process flow of the buckled beams: (a) seed metal deposition, (b) SU-8 patterning, (c) Cu electroplating, (d) SU-8 removal, (e) seed metal removal, and (f) glass substrate etching.

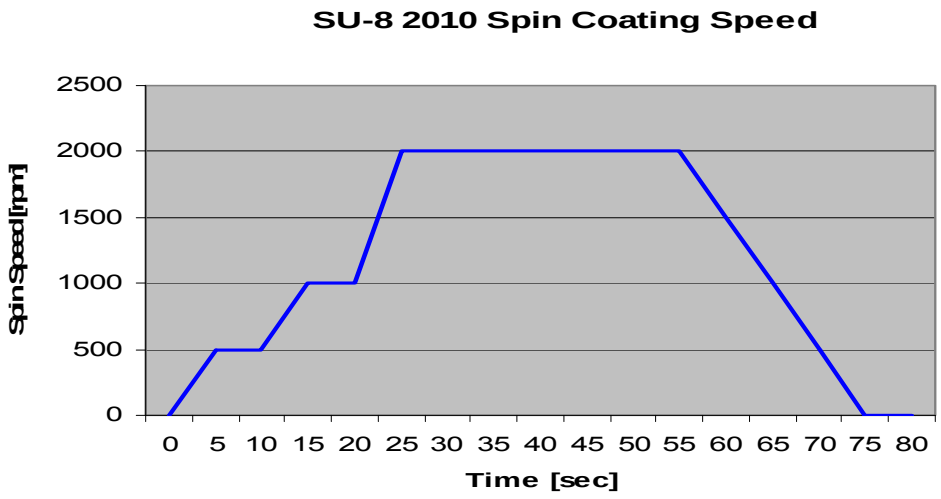

Figure 2.5. SU-8 2010 spin coating parameters

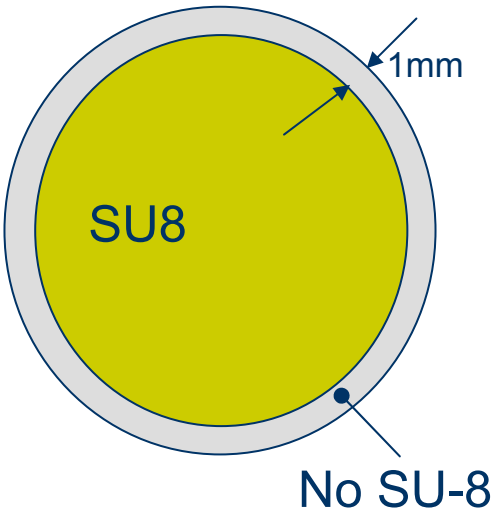

Figure 2.6. The wafer after scraping off the edge beads.

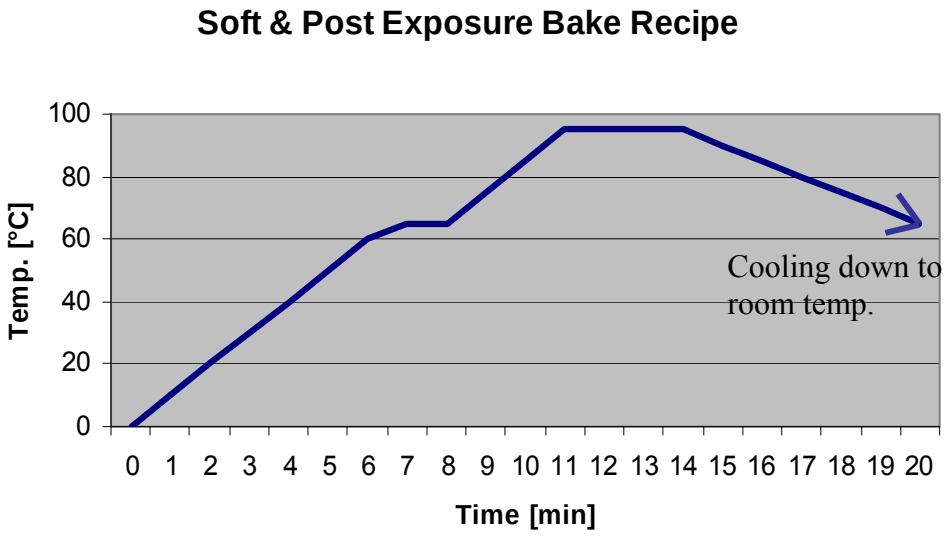

Figure 2.7. A thermal cycle of soft-bake for 10 μm-thick SU-8 2010.

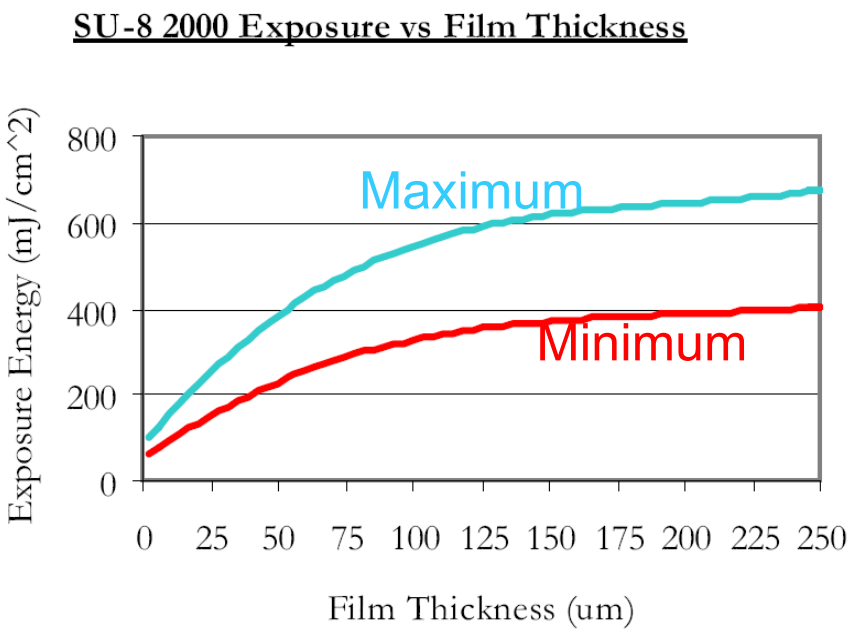

Figure. 2.8. Suggested exposure dose by MicroChem, [2.8].

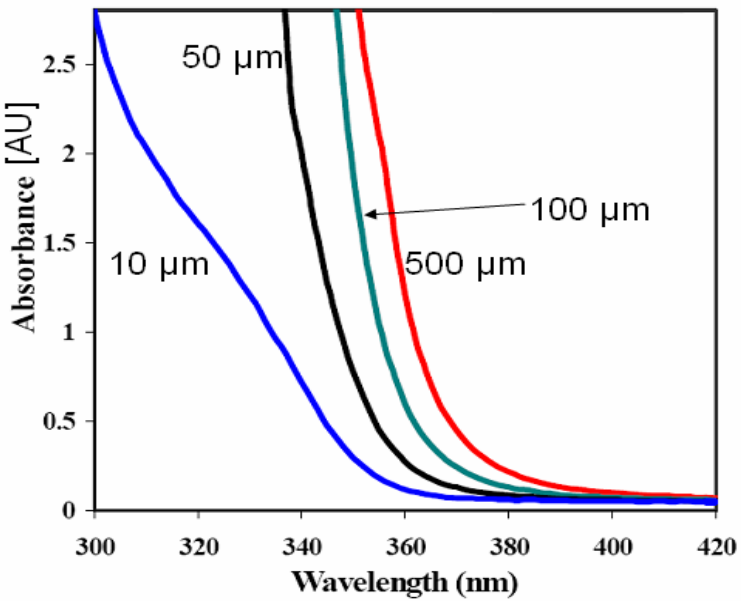

Figure. 2.9. Absorbance vs. wavelength [2.5]

An adhesion problem appeared as shown in Fig. 2.10 when the dose amount was not enough, baking time was short, or SU-8 was coated on particular materials. An adhesion promoter, OmniCoat has been tried, which seemed to solve the problem; however, it was weakened in copper electroplating solution, eventually lifting off SU-8 film during the electroplating process. Alternatively, UV dose amount was increased by 1.5 times, which resulted in good adhesion. When UV dose was further increased to a factor of 2, SU-8 patterns were swollen. Small structures, e.g. 5 μm-wide lines, were severely affected and failed to be fabricated.

2.4.4 Copper Electroplating

Copper was selected as the structural material for its high conductivity (5.96×10^7 S/m), low Young's modulus (110-128 GPa), low residual stress, and good resistance to HF. Electroplating method was chosen for copper deposition considering the thickness of the structure that was designed. Acid-based solution was used for copper electroplating as its composition is shown in table 2.2. Mercaptopropane sulfonic acid (SPS), polyethylene glycol (PEG), and Janus green B (JGB) are additives for better film quality: reduction of the residual stress and improvement of the film density. The conditions for electroplating are described in table 2.3. Both pulse and DC electroplating were attempted. The former provided significantly better topology and uniformity than the latter.

When the current density was below 5 mA/cm^2, non-uniformity of electroplating was severe (Fig. 2.11). For instance, seed layers of wide areas such as contact pads and signal lines were etched out by copper electroplating solution, but narrow patterns such

as buckled beams and ground lines were relatively well plated. Electroplating did not take place at all when even lower DC current was supplied. On the other hand, at higher DC current (10 mA/cm^2), released buckled-beam structures exhibited nontrivial tensile stress as shown in Fig. 2.12. Considering these findings, the electroplating current density was selected as 6.6 mA/cm^2.

In addition to the copper, nickel electroplating was tried as well (composition summarized in table 2.4, performed at 55 °C); however, the electroplated nickel film showed significant tensile stress.

Table 2.2. Copper acid electrolyte solution.

Chemicals	Amount/l	Remarks
Copper Sulfate	150 g	
Sulfuric Acid	50 ml	
Copper Chloride	120 mg	
MPS	10 mg	Brightener
PEG	100 mg	Suppressor
JGB	1 mg	Leveler

Table 2.3. Copper pulse electroplating parameters

	Descriptions		Descriptions
Anode	99.9 % Copper	Duty ratio	50 %
Temperature	RT	Frequency	100 Hz
Total current	20 mA	Growth rate	0.13 μm/min
Current density	6.6 mA/cm^2	Agitation	performed

Table 2.4. Nickel sulfamate electrolyte solution and conditions

Chemicals	Amount/l	Conditions	
Nickel Sulfamate ($Ni(SO_3NH_2)_2$	450 g	PH	4
Boric Acid (H_3BO_3)	37.5 ml	Current Density	6.6 mA/cm^2
Lauryl Sulfate	3 g	Frequency	100 Hz

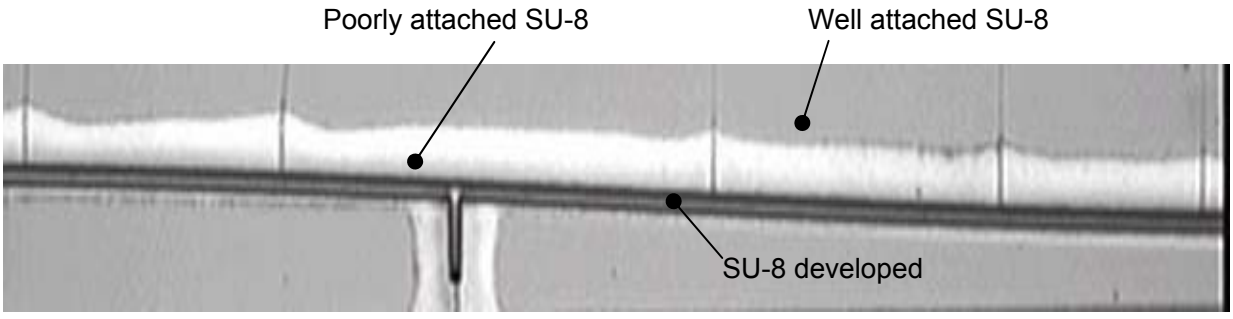

Figure 2.10. Adhesion problem of SU-8 film when processes are not optimized.

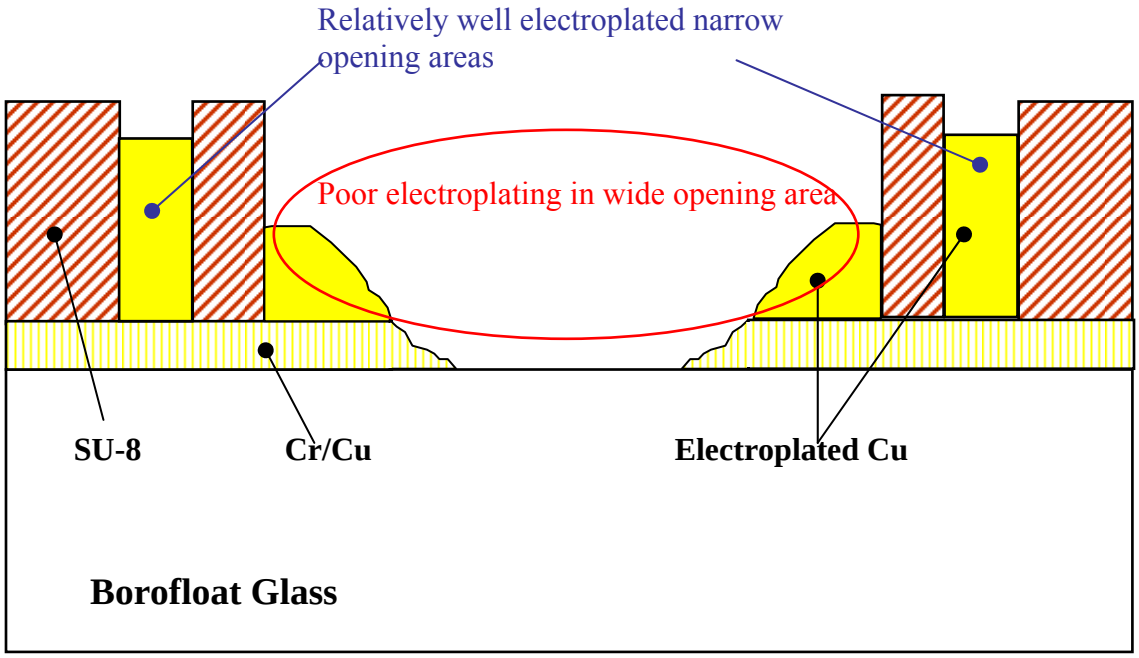

Figure 2.11. Schematic diagram (cross section view) of the electroplated copper when low current density is used.

2.4.5 Removal of SU-8 and Seed layer

After the electroplating process is completed, SU-8 molds were removed by the Nano PG remover for 20 minutes in bath I (60 °C) and for another 20 minutes in bath II (60 °C). For the copper patterns narrower than the adjacent SU-8 molds, SU-8 removal was successfully performed. However, it was difficult to remove the SU-8 resist when the copper pattern was broader than the SU-8 molds because the SU-8 resist was confined between copper patterns and the substrate. The task was even more difficult when copper was plated over the molds resulting in a mushroom shape.

The seed layer was stripped by a mixture of sulfuric acid, hydrogen peroxide, and DI water in 1:1:30 ratios. The etch rate was 2.7 nm/sec. Ti adhesion layer was not

attacked by the mixture but was removed by HF in the subsequent substrate etch process. Etch rate of Ti in HF is known to be very fast (>1 μm/min) [2.10].

2.4.6 Release by Etching of Glass Wafer

The buckled-beams were released by underetching the glass substrate in 49 % concentrated HF. The etch rate was approximately 7 μm/min. The wafer was immersed in HF for 1 minute, rinsed with DI water for 2 minutes, and dehydrated with critical point dryer (CPD). An image of the fabricated buckled beams is presented in Fig. 2.12. In the early experiments, the fabricated buckled-beams showed tensile stress which deprived the beams of bistability. This issue was resolved by reducing the current density and adding additives in the later experiments, which will be discussed in the next section.

2.4.7 Stress Engineering

Two different metals, copper and nickel, were tried for electroplating in this study. As the experiment results correspond with the literatures, nickel was not appropriate for buckled-beam structures. Figure 2.12(a) shows a buckled-beam made of electroplated nickel. By comparing to the traces of the original buckled-beam locations, it is clear that the buckled-beams were deformed due to the severe tensile stress resulting in smaller initial rise than designed.

Kristian, et al. reported that electroplated nickel has tensile stress in the order of 700 MPa [2.11]. This tensile stress value is too high for the beams to have bistability. Stress of electroplated copper film can be significantly lowered by two major factors – current density and additives [2.12, 2.13]. Brongersma, et al. reported that by adding

brightener, tensile stress can be reduced from 80 to 30 MPa, and low current density can also reduce tensile stress [2.13]. Figure 2.12(b) and (c) show the effect of brightener. Buckled-beams in Fig. 2.12(b) (without brightener) are located farther from their traces of the original positions compared to ones in Fig 2.12(c) (with brightener). Distance of a released buckled beam from its original location indicates strength of the tensile stress of the beam. Figure 2.12(c) and (d) show the effect of current density to tensile stress: buckled beams in Fig. 2.12(d) (10 mA/cm^2) moved farther away from their original locations compared to ones in Fig. 2.12(c) (6.6 mA/cm^2).

Since the residual stress of the film has a crucial impact to the bistability of the buckled-beam, stress monitoring patterns (Fig. 2.14, and 2.15) were included in the layout [2.14]. The residual stress σ can be calculated using the distance between the two indicators δ and the following equation [2.15],

$$\sigma = \frac{Ed\delta}{2(1-\nu)l_i l_a} \tag{2.14}$$

where E is the Young's modulus (E_{copper} = 128 GPa), d (20 μm) is the distance between the center of the actuation beams and the rotation center, v is the Poisson ratio (v_{copper} = 0.34), l_a (1000 or 3000 μm) is the length of the actuation beams, l_i (600 μm) is the length of the indicator beams. The stress monitoring pattern with l_a = 1000 μm can measure residual stress between 30 and 300 MPa, and the other one's (l_a = 3000 μm) measurement range is from 10 to 100 MPa. In the case of electroplated copper (current density: 6.6 mA/cm^2, with brightener) the internal tensile stress is measured to be about 6 MPa as shown in the Fig. 2.16.

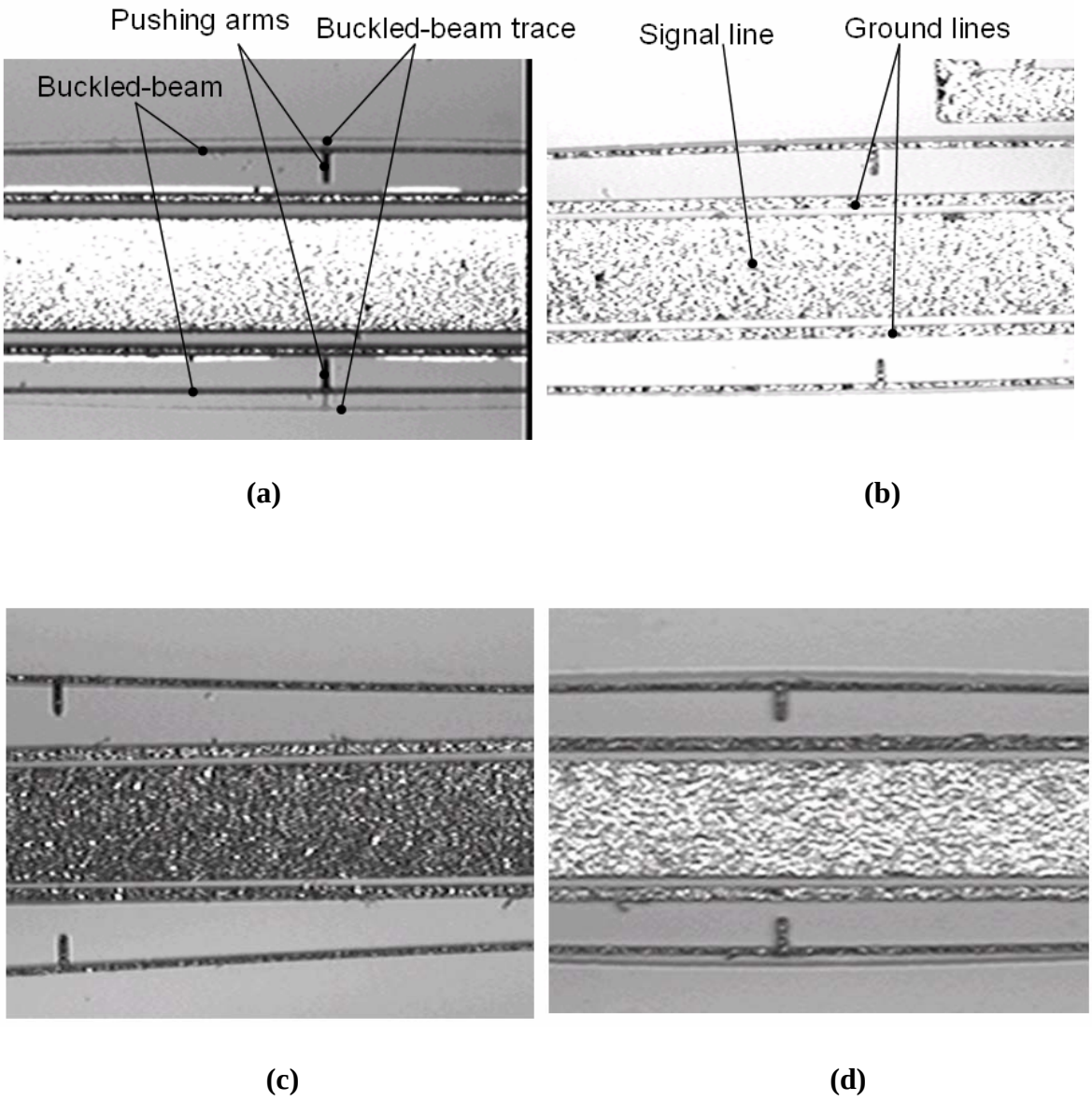

Figure 2.12. Electroplated (a) nickel with 6.6 mA/cm^2, (b) copper without brightener with 6.6 mA/cm^2, (c) copper with brightener with 6.6 mA/cm^2, and (d) copper with brightener 10 mA/cm^2.

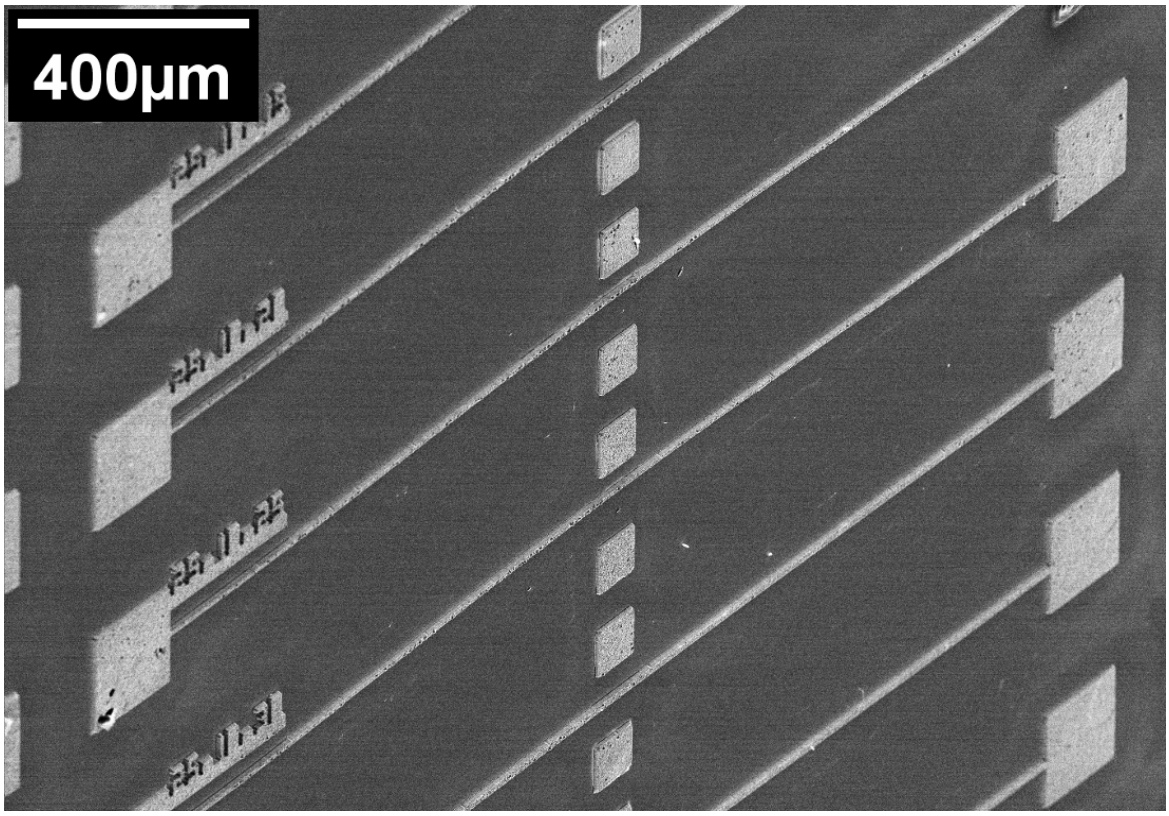

Figure 2.13. An SEM image of the fabricated buckled-beams.

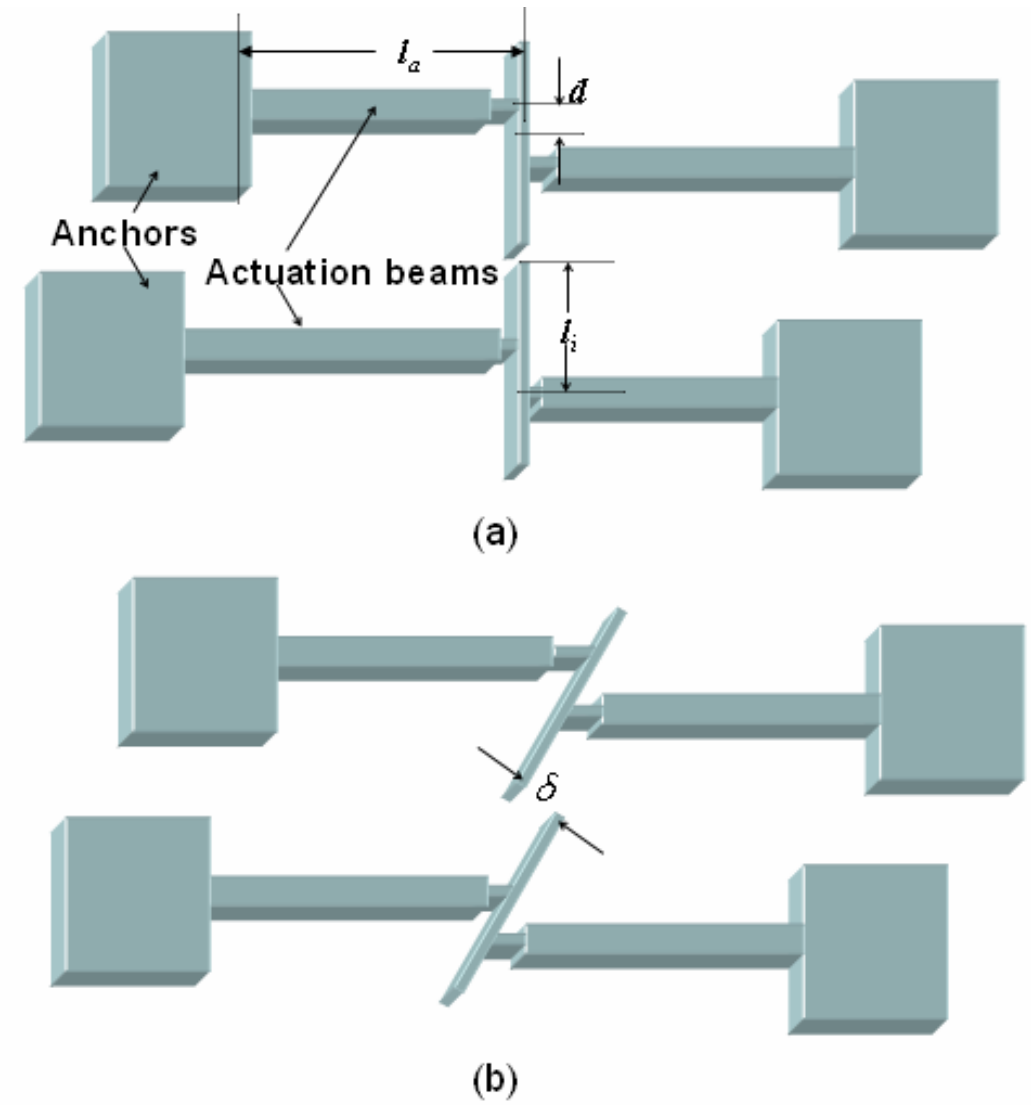

Figure 2.14. Schematic pictures of the stress measurement patterns, (a) before release, and (b) after release when the stress is present on the patterns.

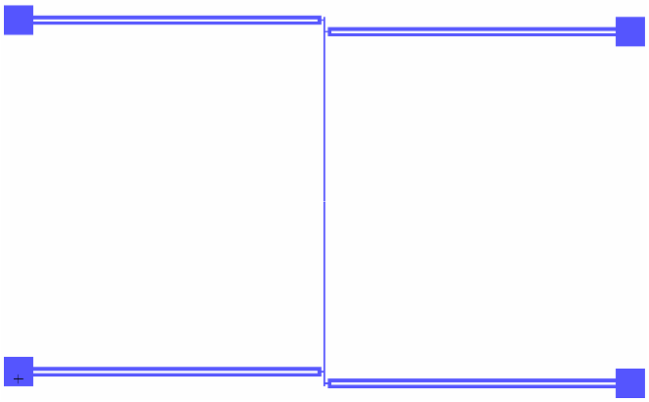

Figure 2.15. L-edit layout of the 1000 μm-long-actuation-beam-stress-measurement pattern

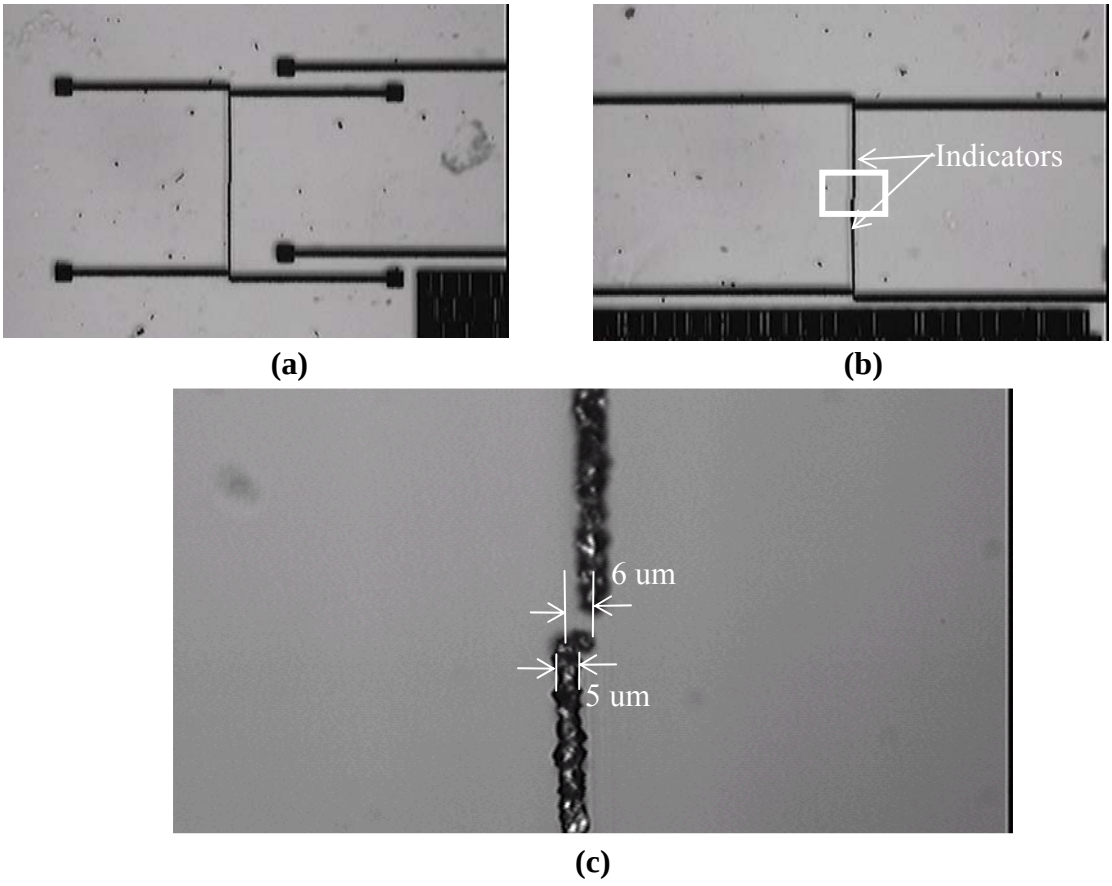

(a) **(b)** **(c)**

Figure 2. 16. Microscopic view of (a) the 1000 μm-long l_a beam, (b) the 3000 μm-long l_a beam, and (c) the indicators of (b).

2.5 Results

2.5.1 Resistance measurement

Resistances of buckled beams have been measured with a setup in Fig. 2.17. A multimeter was connected to buckled beams through probe tips to measure resistance values. Resistivity of electroplated copper was calculated from measured resistance values by equation below,

$$R = 2R_{con} + \rho_{ec}\frac{l_{ec}}{w_{ec}t_{ec}}, \tag{2.15}$$

where, l_{ec}, w_{ec}, and t_{ec} are length, width, and thickness of a measured beam, respectively. For example, resistances of a 1500 μm-long and 5 μm-wide beam (geometric factors, l/wt = 30) and a 3000 μm-long and 5 μm-wide beam (l/wt=60) were 1.5 and 2.1 Ω. Completed measurement results are illustrated in Fig. 2.18. Data point of l/wt = 0 was measured with probing tips as close to each other as possible. The contact resistance (R_{con}) is estimated as 0.45 Ω using (2.15). The resistivity (ρ_{ec}) of electroplated copper is calculated as 2×10^{-8} Ω m. This value is very close to the bulk resistivity of copper, 1.72×10^{-8} Ω m.

2.5.2 Electromagnetic actuation

Electromagnetic actuation of buckled beams was tested using a setup pictured in Fig. 2.17. Bistability of buckled beams were investigated as well. Figure 2.19 shows a buckled-beam actuator (length (l): 3000 μm, initial rise (h): 25 μm) at the two stable states: (a) the first (original, as-fabricated) stable state, and (b) the second stable state. It was experimentally confirmed that a buckled beam with proper dimensions can be

switched between two stable positions by applying the Lorenz force. Magnetic flux density of the permanent magnet used in the experiment was 0.7 T. Switching (critical) currents of buckled-beams with various dimensions were recorded for both forward and backward transitions when snapping was observed (Fig. 2.20). Figure 2.20 also shows calculated switching currents for comparison. The measured switching currents showed good agreement with the calculated ones in general trend. Thinner beams (*t*: 5 μm, Fig. 2.20(a-c)) showed better matching between experiments and theory. Thicker beams (*t*: 10μm, Fig. 2.20(d-e)) required higher switching currents than expected. This phenomenon is thought to be caused by secondary effects which may include electrothermal (Joule heating) effect. When current was applied without external magnetic field, these secondary effects extended a buckled beam so that it bent towards a direction in which it could be elongated. These effects were more severe with yet thicker beams (*t*: 15 μm) as explained in detail in Fig. 2.21. When a low level of current is applied to this 15 μm-thick beam, the secondary effects are more dominant than the electromagnetic effect so that the beam is bent towards the unwanted direction (Fig. 2.21(a)). As the applied current increases, the electromagnetic force overcomes the electrothermal force, and the beam turns its bending direction (Fig. 2.21(c)) until it snaps and passes the second stable position (Fig. 2.21(d)). This is not an ideal situation because it increases required switching current. Moreover, most of those thick beams (*t*: 15 μm) went through permanent deformation, and eventually failed to operate because once the beam flips, the secondary force is in the same direction as the electromagnetic force, resulting in large deformation at an elevated temperature.

Effects of length and thickness of buckled beams on switching current are illustrated in Fig. 2.22 and Fig. 2.23, respectively.

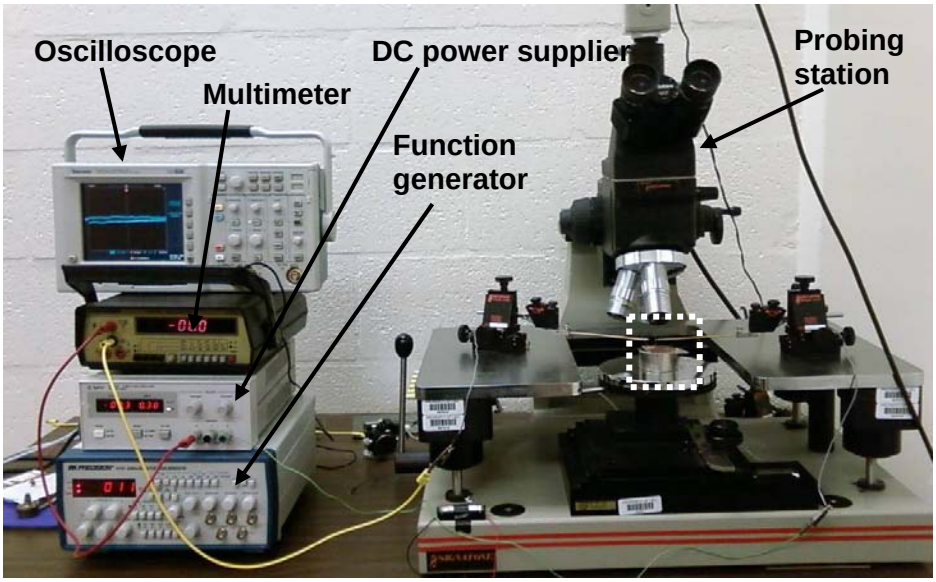

(a)

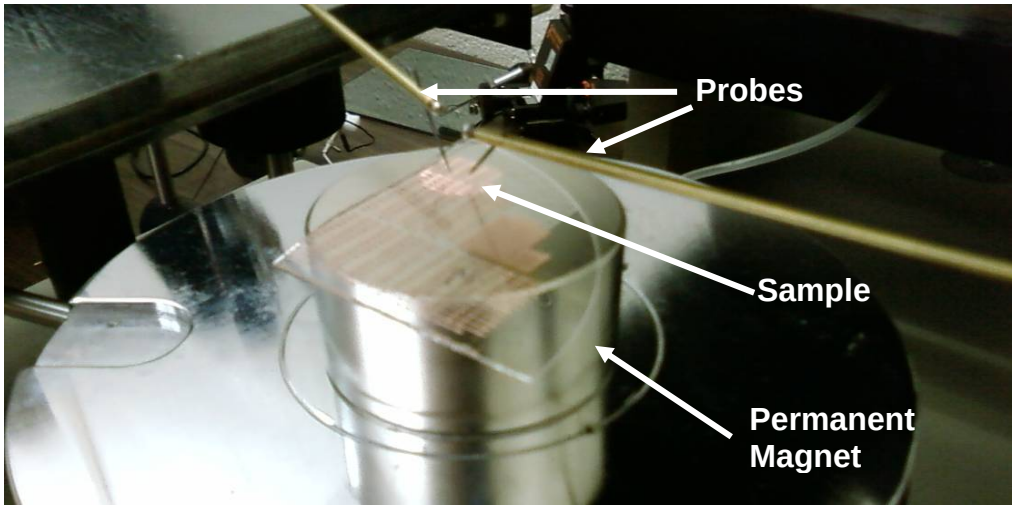

(b)

Figure 2.17. Pictures of (a) a DC measurement set up, and (b) a close up view of the box in (a).

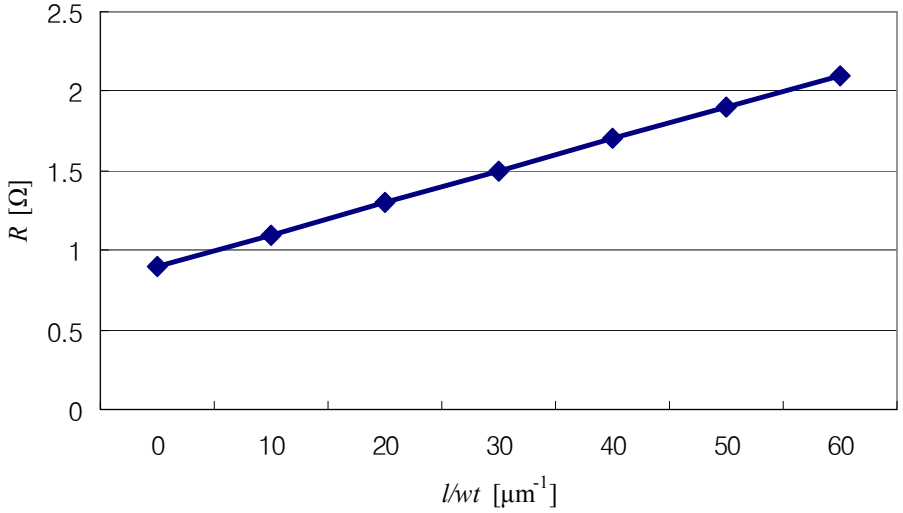

Figure 2.18. Measured resistance, plotted as a function of *l/wt*.

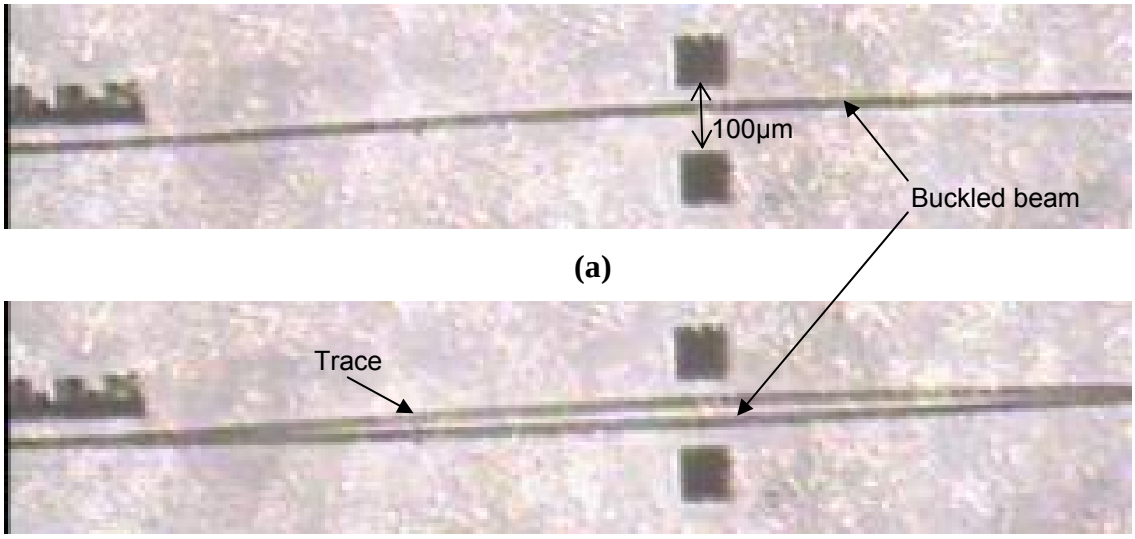

Figure 2.19. Images of a buckled beam at (a) the first, and (b) the second stable positions. Trace of the buckled beam can be also seen in (b), which is produced during a release etching step.

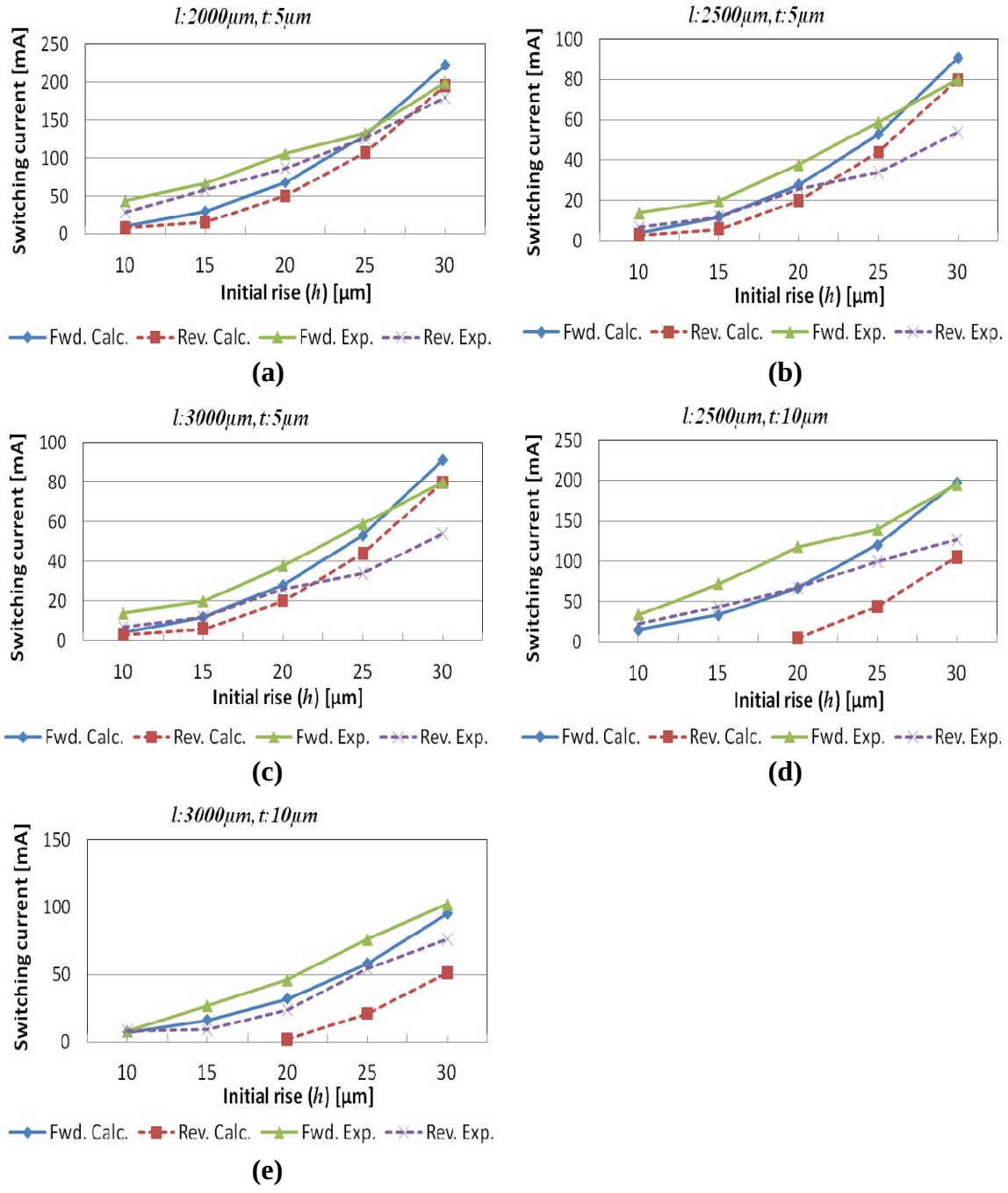

Figure 2.20. Calculated and measured switching currents of buckled-beam actuators with dimensions of (a) length (*l*): 2000 μm, thickness (*t*): 5 μm, (b) *l*: 2500 μm, *t*: 5 μm, (c) *l*: 3000 μm, *t*: 5 μm, (d) *l*: 2500 μm, *t*: 10 μm, and (e) *l*: 3000 μm, *t*: 10 μm. For all devices, width of the beam is 10 μm and magnetic field intensity (B) is 0.7 T.

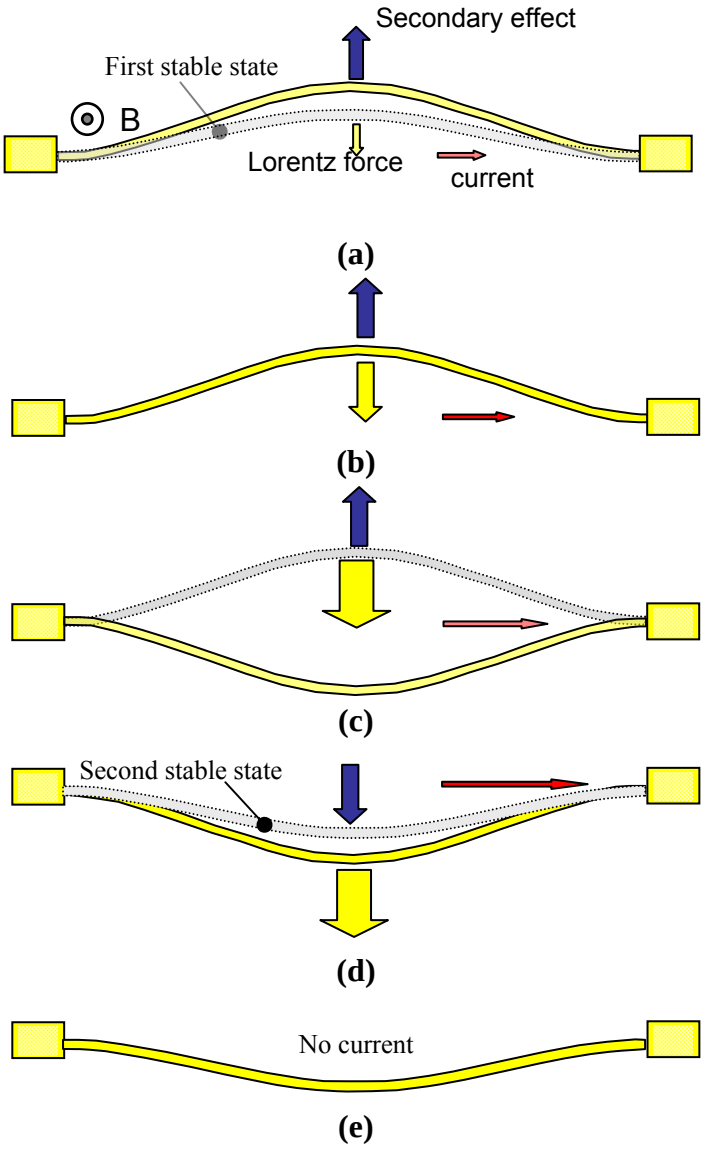

Figure 2.21. Schematic diagrams of movement of a short buckled beam when both electromagnetic and secondary effects present. Applied current increases gradually from (a) to (d). The beam (a) bends upward (secondary force > electromagnetic force), (b) reaches the equilibrium (secondary force = electromagnetic force), (c) changes the bending direction (secondary force < electromagnetic force), (d) snaps towards and passes the second stable position (secondary and electromagnetic forces are in the same direction), and (e) stays in the second stable position when current is withdrawn.

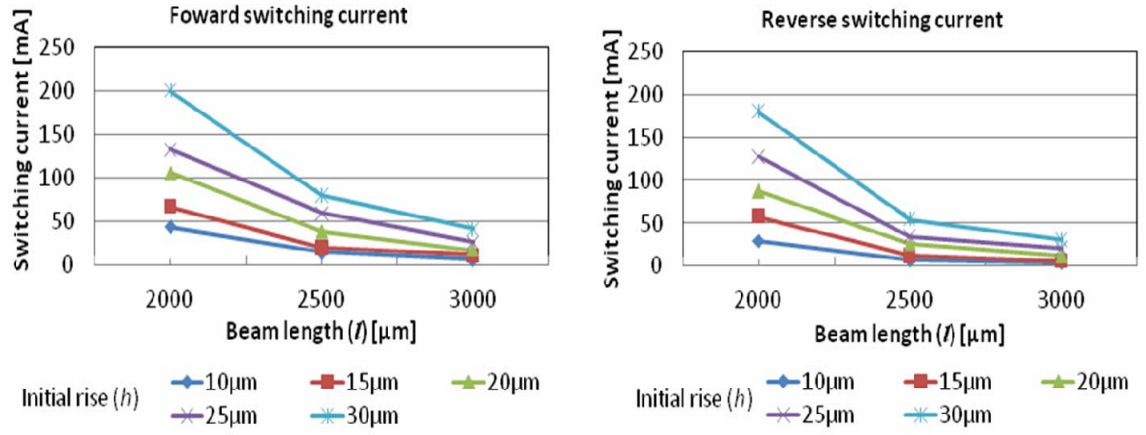

(a) **(b)**

Figure 2.22. Measured switching currents of buckled-beam actuators for various beam lengths and initial rises. (a) forward, and (b) reverse switching currents. For all devices, thickness of the beam is 5 μm.

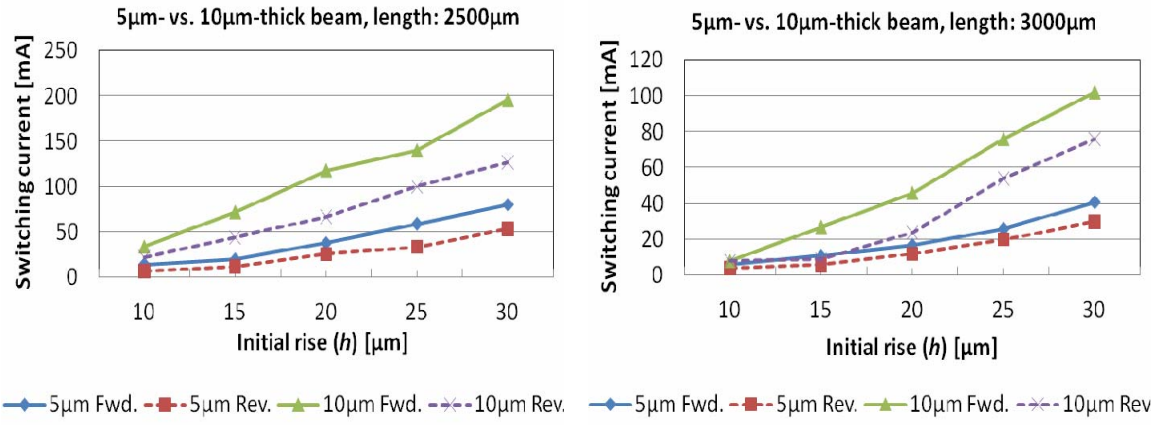

(a) **(b)**

Figure. 2.23. Comparison of measured switching currents between a 5 μm- and a 10 μm-thick beams. Length: (a) 2500 μm, and (b) 3000 μm.

2.6 Summary and further works

Bistable electoromagnetic actuators have been designed and fabricated using SU-8 UV-LIGA and copper electroplating processes. Beams with various dimensions were actuated by current range of 10 to 200 mA which corresponds to voltage range of 20 to 400 mV. Driving force ranged from 10 to 200 μN and corresponding displacement was from 20 to 60 μm. Since the actuator consumes no power at each of the stable states, it is very useful in low power applications. Its low operation voltage makes it compatible with the CMOS circuits. Performance of the proposed actuators outweigh other actuators with high force, low power consumption, fast actuation speed, low actuation voltage. It is highly suitable for an RF MEMS switch application.

To increase driving force of buckled-beam actuators, one can increase the beam thickness. But, as explained in the previous section, this makes the **secondary** effects more severe. Instead, double- or more-beam configuration with connection bars in the middle can be used (Fig. 2.24) for the same purpose without severing the secondary effects.

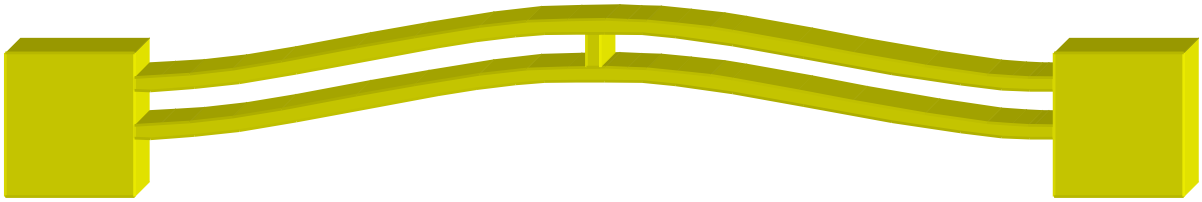

Figure 2.24. Schematic drawing of a double-buckled-beam actuator for increased driving force.

CHAPTER III. LATERALLY DRIVEN RF MEMS SWITCHES

3.1 Operation principle

The developed buckled-beams as described in the chapter II were incorporated to an RF MEMS switch design. Fig. 3.1 shows the schematic drawings of the proposed switch. The basic structure of the proposed switch is a combination of a coplanar waveguide and two buckled-beam actuators. The coplanar waveguide has a ground-signal-ground (GSG) configuration and its dimensions were designed for 50 Ω characteristic impedance over broad RF band. Details of the coplanar waveguide (CPW) design are provided in the section 3.3. While the signal line is immobile sitting on a glass substrate, the ground lines are clamped-clamped movable beams. On each side of the ground lines, an electromagnetically actuated, bistable buckled-beam is located.

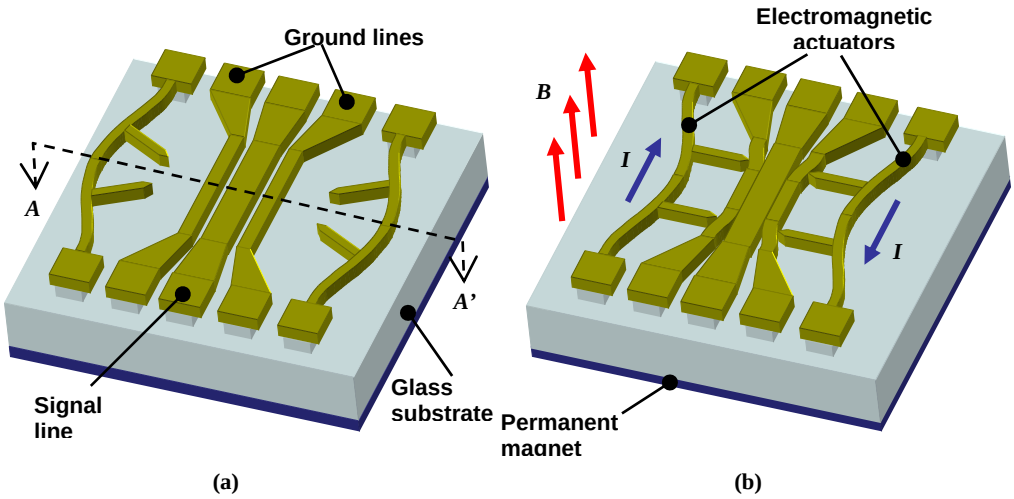

Figure 3.1. Schematic drawings of the proposed RF MEMS switch (a) at the on-state and (b) at the off-state.

In the original (as-fabricated) state (Fig. 3.1(a)), the actuators are detached from the ground lines, and hence exert minimum influence on the coplanar waveguides, which is referred as the "on-state" because the RF signal can flow unperturbed except a small loss in this state. As currents flow through the actuators as depicted in Fig. 3.1(b), the actuators move towards the ground lines by the Lorentz force and if the currents are high enough to move the actuators beyond the critical displacements, they push the ground lines to be contacted with the signal line, which is called as the "off-state" because now most of the RF signal is reflected due to this low impedance section that causes severe impedance mismatch. Due to bistability of the buckled-beams, the ground lines and the actuators do not return to their original positions when the currents are removed. To move the actuators back to their original positions and change the state of the switch from "off" to "on", reverse currents have to be applied to the actuators. To prevent DC connection between the ground lines and the signal line, and between the ground lines and the actuators, insulation material, parylene C is deposited on the sidewalls of all the structures.

In the proposed switch, electromagnetic bistable buckled-beam actuators are used, because they reduce actuation voltage, give enough force to push the ground lines, and do not need force to keep either on or off states.

3.2 Merits

The proposed switch has several advantages compared to the conventional capacitive-type RF MEMS switches. Since the electromagnetic actuation mechanism is adopted in the proposed switch, required actuation voltage is much lower than the

electrostatic actuation mechanism. Reported conventional capacitive-type RF MEMS switches with the electrostatic actuators usually require operation voltages higher than 20 V, sometimes reaching over 100 V [3.1]. Therefore, many of them need to be accompanied by high voltage drive chips in order to be integrated with the other low-voltage components. However, the electromagnetic actuators used in the proposed switch demand less than 1 V. A usual drawback of high power consumption of the typical electromagnetic actuators is not an issue for the proposed switch due to bistability of the buckled-beam actuators.

As shown in Fig. 3.1, all of the structures can be made out of the same layer so that only one mask is necessary for the entire process. This single-mask-process feature with simple fabrication steps is beneficial with dramatically reduced production cost and improved production yield as production of the device does not require an expensive mask aligner.

The device can be fabricated by low-temperature processes, which makes it compatible with the Monolithic Microwave Integrated Circuit (MMIC) processes. The processes are not particularly dependent on the substrates, and hence the switch can be made on various substrates.

Conventional capacitive-type RF MEMS switches suffer from trapped charges in the dielectric layer, which undesirably attract the membrane and bring about return loss or even failure [3.2]. However, in the proposed switch, the trapped charge issue is dramatically diminished because the actuators are separated from the coplanar waveguide, very low voltage is applied to the actuators, and the polarity of voltage on

the actuators is continuously toggled – e.g., if one end of the actuator is grounded and positive voltage is applied to the other end for the switch "off" operation, in the next sequence, negative voltage is applied to the other end to return the switch back to the "on" state.

Another issue in the conventional capacitive-type RF MEMS switches is series inductance that significantly aggravates the off-state isolation performance through electrical resonance. Figure 3.2 shows an equivalent circuit diagram of a capacitive-type RF MEMS switch. A membrane of the conventional switches bridging the signal line and the ground lines creates high enough series inductance (L_s) to result in narrowband off-state RF characteristics. Using the equivalent circuit diagram (Fig. 3.2), the impedance (Z_s) of the switch section can be expressed as,

$$Z_s = R_s + j\omega L_s + \frac{1}{j\omega C_s} \tag{3.1}$$

$$\approx \begin{cases} (j\omega C_s)^{-1} & \text{for } f << f_0 \quad (3.2) \\ R_s & \text{for } f = f_0 \quad (3.3) \\ j\omega L_s & \text{for } f >> f_0 \quad (3.4) \end{cases}$$

where, $f_0 = \dfrac{1}{2\pi\sqrt{L_s C_s}}$

and the input impedance of the switch is,

$$\boldsymbol{Z_{in} = \left(Z_0 \| Z_s \right) = \frac{Z_s Z_0}{Z_s + Z_0}} \tag{3.5}$$

where, Z_0 is the characteristic impedance of the coplanar waveguide. Then, the S_{21} is,

$$S_{21} = \frac{2Z_{in}}{Z_{in} + Z_0} = \frac{2Z_s}{2Z_s + Z_0}, \tag{3.6}$$

and the isolation at the off-state is expressed as,

$$Isolation = 10 \cdot \log \left| S_{21} \right|^2 . \tag{3.7}$$

At the electrical resonance frequency (f_0), Z_s has its minimum value resulting in maximum isolation. But, as the frequency departs from f_0, the isolation becomes worse. Hence, low electrical resonance frequency leads to narrowband RF characteristics. Figure 3.3(a) shows the calculated isolation characteristics for various series inductance values. The effect of the inductance is prominent.

Series inductance of the proposed switch is negligible because the ground lines directly contact the signal line. Hence, the frequency of interest is way below the electrical resonance frequency. Since the series resistance of the proposed switch is very small. Therefore, the isolation formula can be simplified as,

$$\begin{aligned} isolation &= 10 \cdot \log \left| \frac{1}{1 + j\pi f C_s Z_0} \right|^2 \\ &= 10 \cdot \log \frac{1}{1 + \pi^2 f^2 C_s^2 Z_0^2} \end{aligned} \tag{3.8}$$

The off-state capacitance can be calculated as,

$$C_s = \frac{2 \cdot \varepsilon_0 \cdot \varepsilon_r \cdot t_{GND} \cdot l_{contact}}{d} . \tag{3.9}$$

The parameters of the above equation are as follow; ε_0: permittivity in free space, ε_r: relative permittivity of parylene C, t_{GND}: vertical thickness of the ground lines, $l_{contact}$: contact length of the ground line and the signal line, d: distance between the signal line

and the ground line, and *f:* frequency. Figure 3.3(b) shows the calculated isolation for various contact lengths, $L_{contact}$ from DC to 40 GHz with R_s = 0.1 Ω and L_s = 1 pH. When the contact length is 2 mm, the isolation is better than 40 dB at 40 GHz.

Another serious issue of the RF MEMS switch is the power handling capability. Due to the skin effect, RF current is concentrated along the edges of the conductors, and for high power (>1 W) RF signal, the peak current density can surmount the critical current density with the usual geometries. To keep the current density below the critical value of the particular material, the coplanar waveguide has to be built taller, which cannot be readily done in the conventional switches, for the huge step height can make the later processes difficult. On the other hand, the proposed switch does not suffer from this limitation but can have tall conductors as long as the electroplating mold can afford the height.

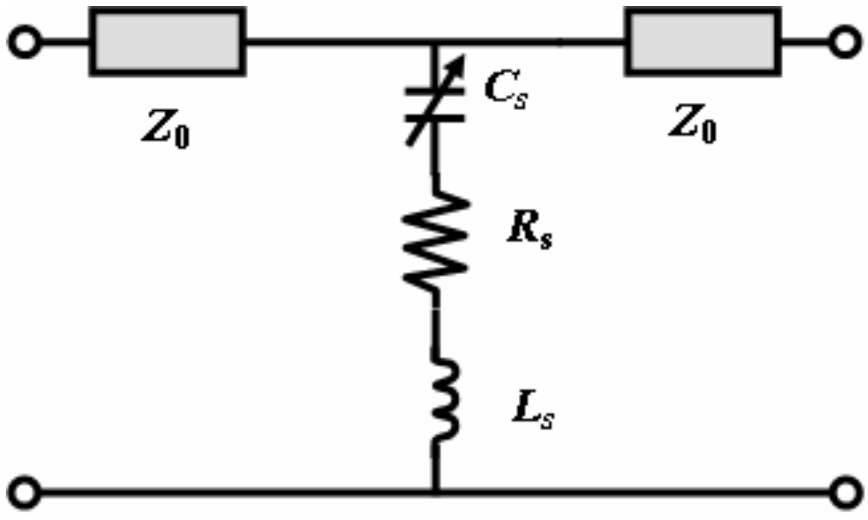

Figure 3.2. The equivalent circuit diagram of the capacitive-shunt type switch.

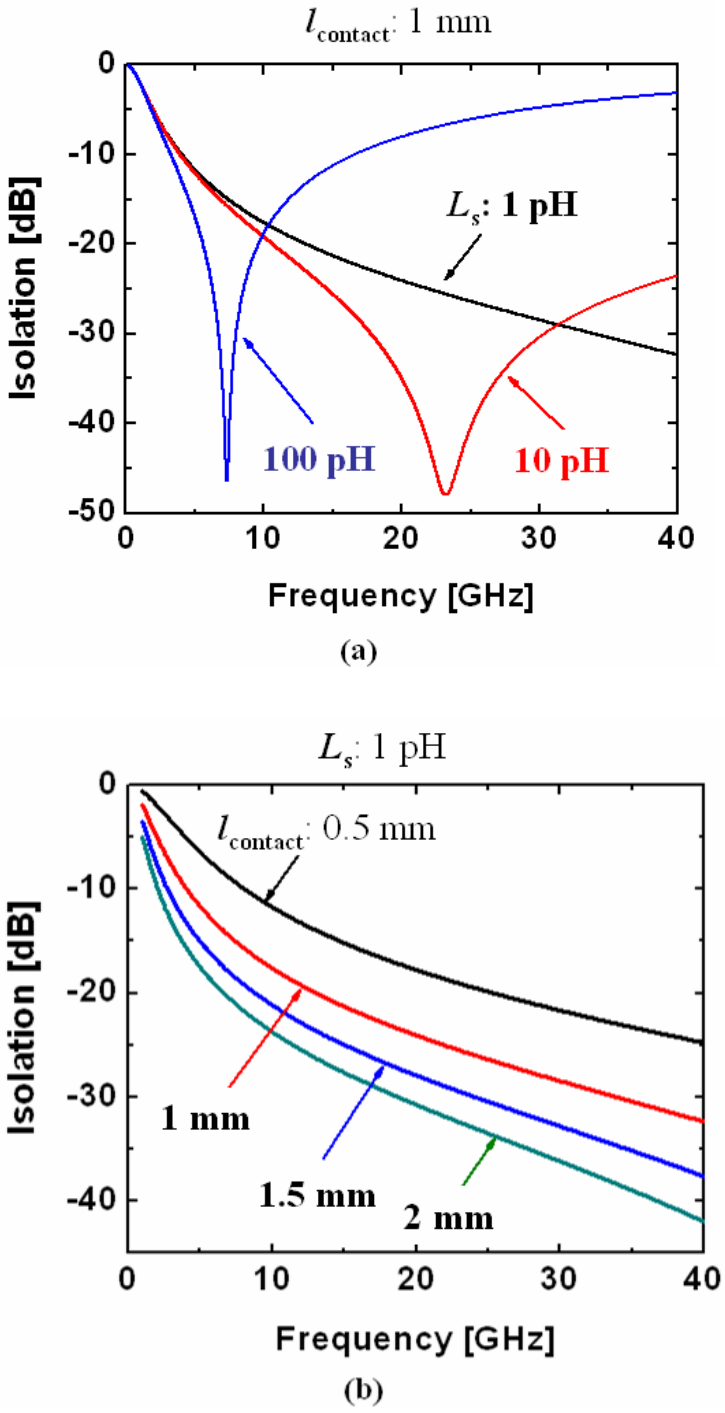

Figure 3.3. Calculated isolation as a function of frequency for various (a) series inductances, and (b) contact lengths ($L_{contact}$). R_s = 0.1 Ω is used for the calculation.

Another issue related to the high RF power is the unwanted modulation of the movable part by the high DC voltage component of the signal. The proposed switch can resist better to this high DC voltage because its movable part that is subject to the induced electrostatic force has much higher aspect ratio (gap over width) compared to that of the conventional switches.

As most of the conventional RF MEMS switches, the proposed switch is also expected to show high linearity (IP_3>+80 dBm) and low insertion loss (<1 dB).

3.3 Design of coplanar waveguides

Among various kinds of waveguides available in microwave frequency range, a coplanar waveguide (CPW) is most frequently used, in monolithic microwave integrated circuits (MMICs) for its planar configuration. Having ground lines and a signal line side by side, it is also a preferred waveguide type for capacitive-shunt type switches. Its general structure is ground-signal-ground lines (GSG) on a dielectric substrate as shown in Fig. 3.4(a). One significant deviation of a CPW part of the proposed switch from a conventional CPW is that the ground lines are floated over the substrate with about 5 μm of air gaps (Fig. 3.4(b)), so that they can be deformed by actuators. For reasonable mechanical compliance, a center part of the CPW, or a modified CPW section of the proposed switch is designed to have narrower lines and gaps than outer parts. Dimensions of the outer parts were decided considering microwave on-wafer probing and robust mechanical anchoring. Between the center part and the outer parts, line widths and gaps are gradually changed to minimize impedance-mismatch-induced signal reflection.

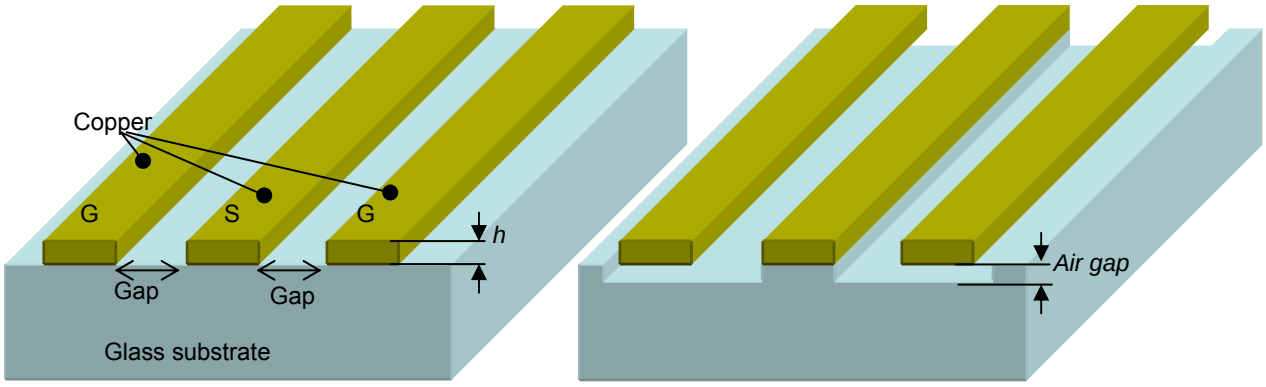

(a) (b)

Figure 3.4. Sketches of coplanar waveguides (CPW). (a) a conventional CPW, and (b) a modified CPW for the proposed switch.

For general 50 Ω impedance matching with external circuits, all sections of the CPW of the proposed switch were designed to have 50 Ω characteristic impedance at on-state. Characteristic impedance of CPWs depends on dimensions of signal line, ground lines, gap between them, and dielectric constant of the substrate. Due to the unusual structure of the CPW in the proposed switch, a finite-element-method-based numerical simulation program, the Sonnet Suit Lite [3.3] was used for design and analysis. Figure 3.5 shows an example of a 3-D drawing and calculated current density of a CPW using the software.

First, characteristic impedance was calculated for various dimensions using the Sonnet Suit Lite ignoring effect of metal thickness because the actual metal thickness was beyond the limit that is permitted with the Lite version of the Sonnet Suit. Then, the results were modified using a web-based CPW calculator [3.4]. Figure 3.6 shows

calculated results of characteristic impedance as a function of gap between a signal line and a ground line for various frequency. It shows that characteristic impedance does not vary much over broad frequency ranges (10-40 GHz), but decreases exponentially as the gap becomes closer. An effect of finite width of ground lines was investigated as the results are depicted in Fig. 3.7. As ground lines become narrower, both return loss ($|S_{11}|^2$), and insertion loss ($|S_{21}|^2$), increase. Considering this effect and mechanical compliance, ground line width of the main part of the switch was optimized at 10 μm while signal line width and a gap between a signal line and a ground line were designed as 100 μm and 10 μm, respectively. Layout of a CPW part of the switch is shown in Fig. 3.8(a).

To verify the simulation results and to experimentally search the optimum dimensions, modified CPWs (Fig. 3.8(a)) with various dimensions are included in the mask layout. A number of conventional CPWs (Fig. 3.8(b)) are added to the mask layout as well for comparison. Table 3.1 summarizes values of the CPW parameters used in the mask layout.

Table 3.1. Coplanar waveguide dimensions (unit: μm)

	Signal line width	Ground line width	Gap spacing
Modified	50, 60, 70, …, 150	5, 10, 20	1, 5, 10, 15, 20
Conventional	50, 60, 70, …, 150	150	5, 10, 15, …, 30

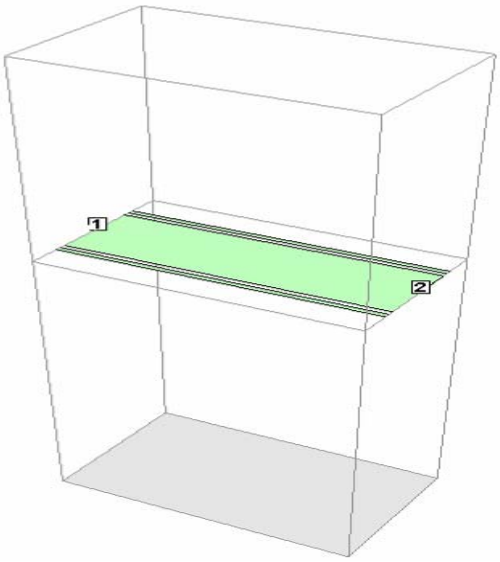

(a)

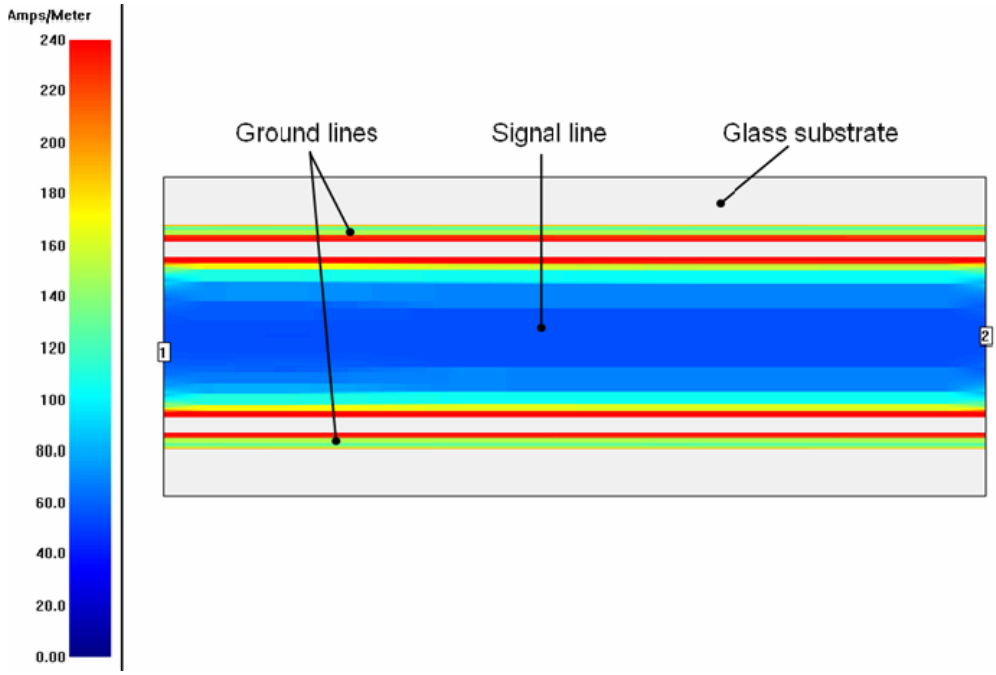

(b)

Figure 3.5. Sonnet Suit Lite (a) 3D view, and (b) current density of designed coplanar waveguide.

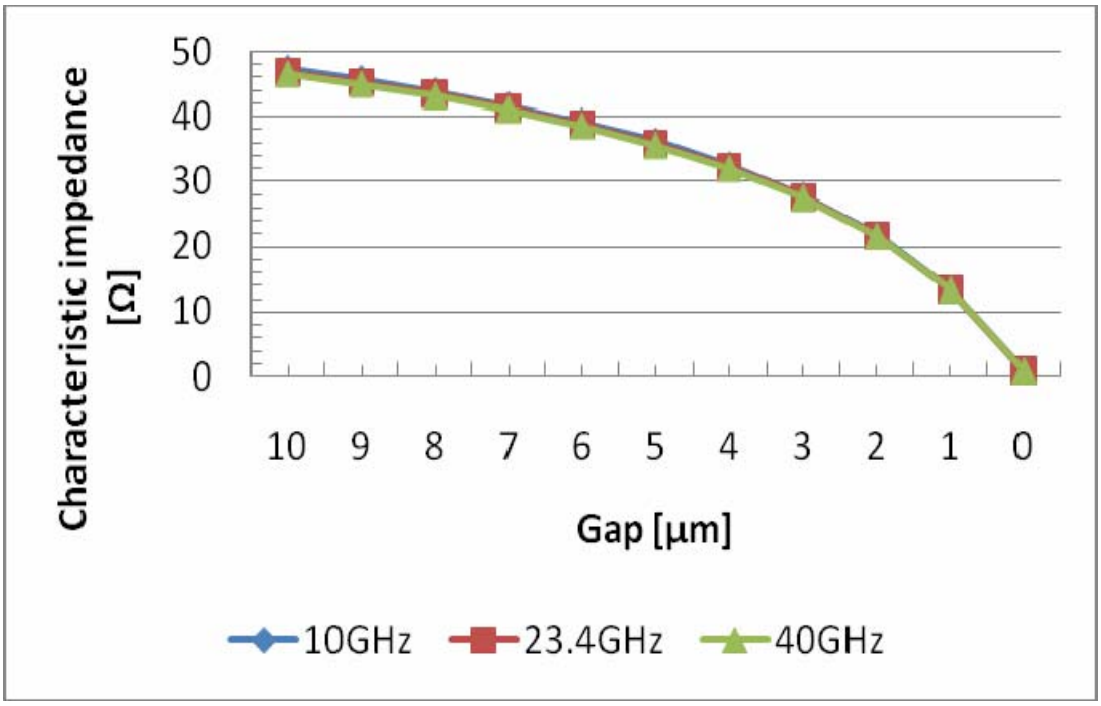

Figure 3.6. Calculated characteristic impedance (Z_0) as a function of a gap between a signal line and a ground line for various frequencies. Signal line width: 100 μm, ground line width: 10 μm, air gap underneath ground lines: 10 μm, thickness of metal lines: 10 μm.

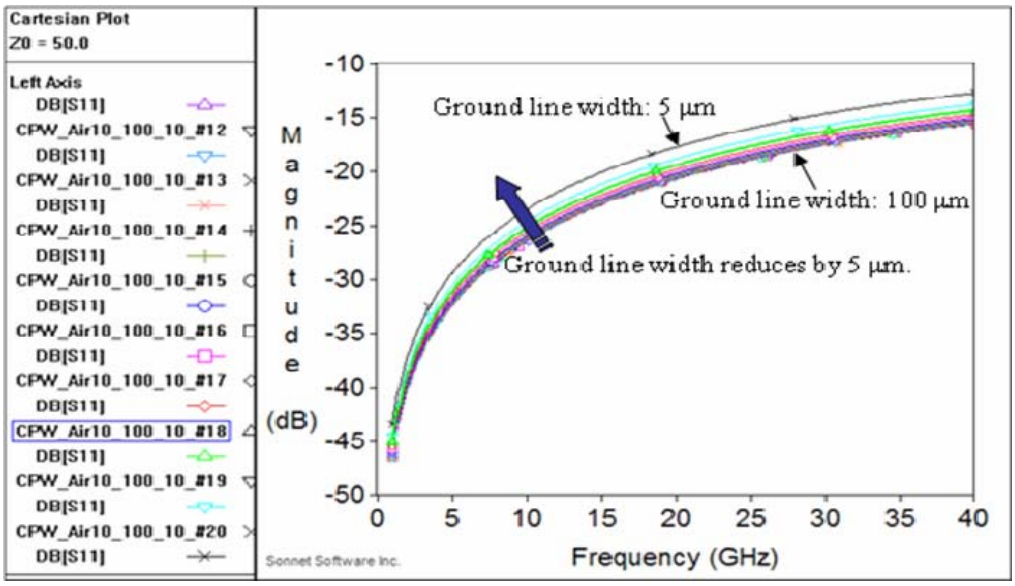

(a)

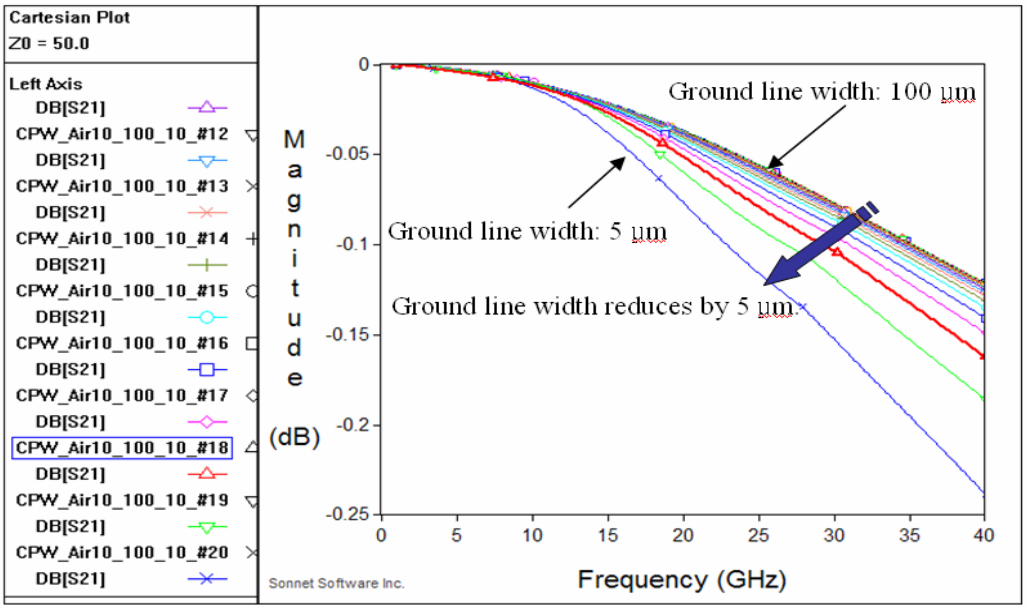

(b)

Figure 3.7. S-parameter calculation results of CPWs using Sonnet Suit Lite for various ground line widths. Signal line width: 100 µm, air gap underneath ground lines: 10 µm, thickness of metal lines: 10 µm. (a) S_{11}, and (b) S_{21}.

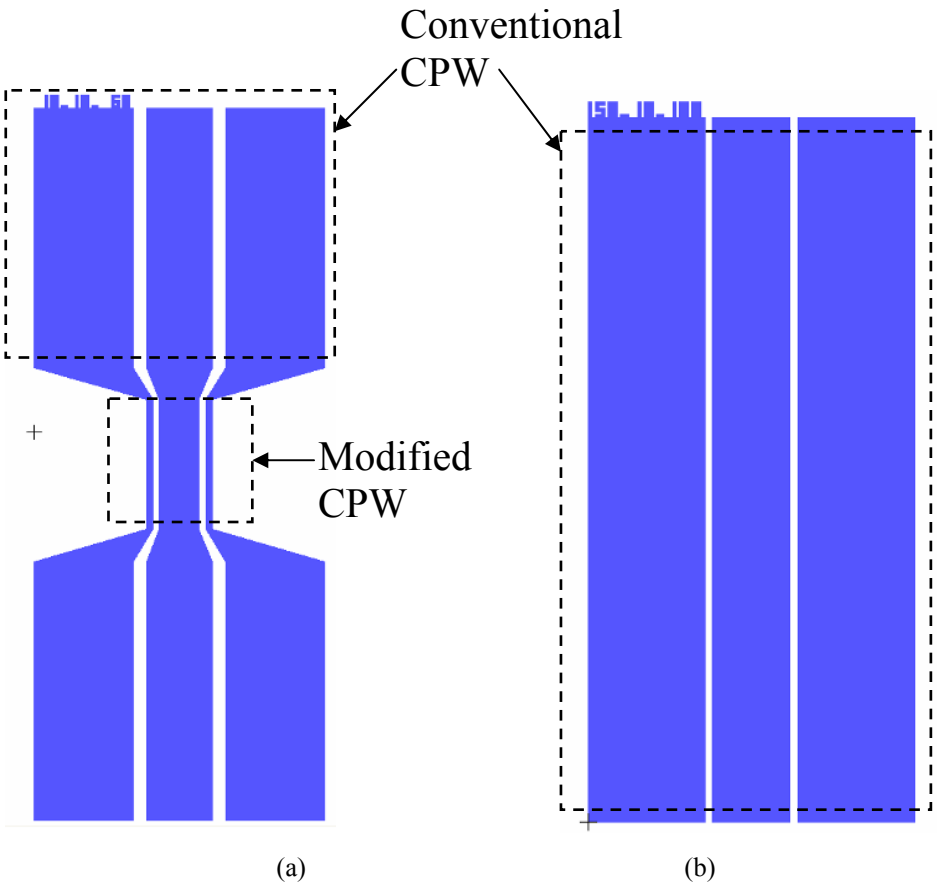

Figure 3.8. Layouts of selected CPWs. (a) A modified CPW and (b) a conventional CPW.

3.4 Mechanical analysis

Mechanical analysis of the proposed switch is an extension of that of the buckled-beam actuators presented in the section 2.2. In that analysis, no constraint was specified with regard to deformation of the buckled beams. As a load greater than the forward critical load is applied, the buckled beam is snapped to pass a region of negative slope and reaches a point beyond second stable position. When the load is withdrawn, it settles at the second stable position. What makes the proposed switch different from a free buckled-beam actuator in mechanical point of view is a ground line that is pushed towards a signal line by the buckled-beam actuator. When the ground line is pushed, it pushes back the buckled beam as it has an elastic property. Therefore, this effect has to be taken into consideration in mechanical analysis.

Whether or not the ground line makes contact with the signal line is dependent on relative strength of applied load, restoring force (F_b) of the buckled beam, and restoring force (F_{GND}) of the ground line. When the applied load is removed in this situation, it is F_b what balances F_{GND}. The switch has to be designed so that F_b is large enough to push the ground line to make a contact with the signal line even when no load is applied (Fig. 3.9(a)). If F_b is not sufficiently large, the ground line will fail to make a contact with the signal line as illustrated in Fig. 3.9(b). In that case, a small amount of load (i.e. current) has to be applied to complete the contact. If F_{GND} is larger than the backward critical load (F_{crb}: similar to q_{crb} described in the section 2.2 except that applied load is a point load), the ground line sends back the buckled-beam to its original stable position and becomes flat as if unperturbed.

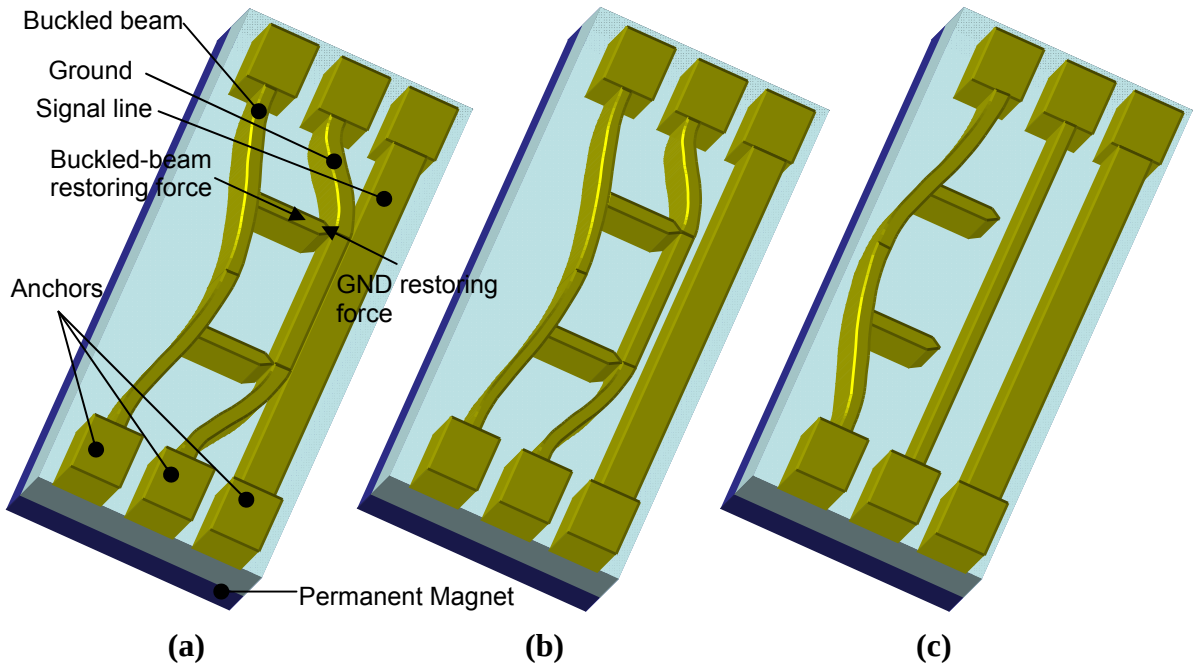

Figure 3.9. Schematic drawings of the proposed switch when (a) $F_{contact} < F_b$, (b) $F_b < F_{crb}$ and F_{con}, and (c) $F_{GND} > F_{crb}$. $F_{contact}$ is restoring force of a ground line when it makes a contact with a signal line. F_b is restoring force of a buckled-beam actuator. F_{GND} is restoring force of a ground line. F_{crb} is a backward critical load. F_{GND} and F_b are function of displacement of a ground line, and a buckled-beam.

In order for the buckled beam to be able to push the ground line, the location of the flat ground line has to be overlapped with the buckled-beam's second bistable position. Because they cannot be physically overlapped, as depicted in the Fig. 3.10, the ground line is bent in the +*y*-direction while the buckled beam cannot reach its second bistable position, which can be considered as it is deformed in the –*y*-direction. As can be seen from the Fig. 3.10, summation of maximum deformation of the ground line (d_{GND}), and the deformation of the buckled beam at the pushing arms (d_b) is equal to the overlap distance (d_{OL}) between them. The backward critical deformation of the buckled beam is defined as d_{crb}.

The ground line consists of a bending part and a flat part as shown in Fig. 3.11(a). The flat part is where the ground line makes a contact with the signal line. It does not contribute to the restoring force so that it can be ignored in the force calculation and the ground line can be simplified as depicted in Fig. 3.11(b). If the ground line is deformed with maximum displacement of d_{GND}, the corresponding restoring force is,

$$\boldsymbol{F_{GND} = \frac{192 E I_{GND}}{L_{bend}^3} \cdot d_{GND} = \frac{192 E I_{GND}}{L_{bend}^3} \cdot \left(d_{OL} - d_b \right)}, \tag{3.10}$$

where E is the Young's modulus of copper and L_{bend} is the length (2000 μm) of the bending section. I_{GND} is the moment of inertia which can be described as,

$$I_{GND} = \frac{w_{GND} \cdot t_{GND}^{\ 3}}{12}, \tag{3.11}$$

where w_{GND} and t_{GND} are the width (10 μm) and thickness (10 μm) of the ground line, respectively.

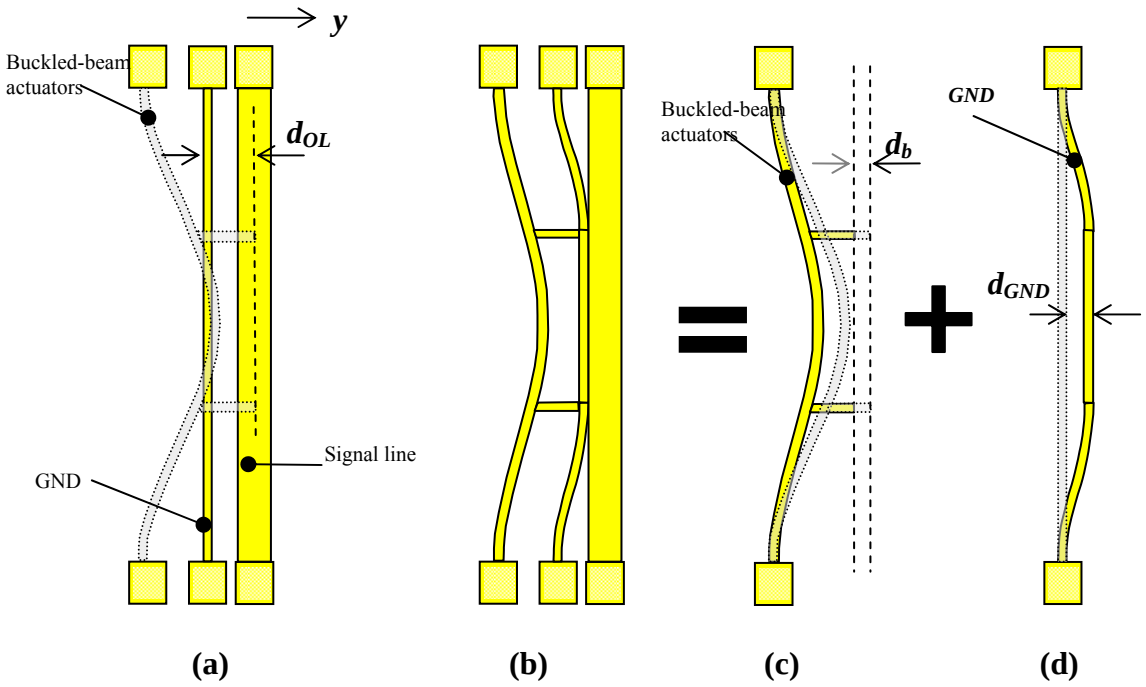

Figure 3.10. Schematic diagrams illustrating contact of a ground line and a signal line while the former is pushed by a buckled-beam actuator. (a) Shape and location of the buckled-beam in a second stable state is drawn in dotted lines as if the signal and the ground lines are not present. Distance between the right end of the pushing arms of the buckled beam and the left end of the ground line is the overlap distance between two (d_{OL}). (b) The buckled-beam pushes the ground line so that it makes a contact with the signal line. This diagram is decomposed into (c) and (d). (c) The buckled-beam part only from the diagram (b). It also shows its ghost image when it does not push the ground line. Distance between two is defined as d_b. (d) The ground line part only from the diagram (b). It also shows its ghost image when it is not pushed by the buckled beam. Distance between two is defined as d_{GND}. $d_{OL}=d_b+d_{GND}$.

Deformation of the buckled beam can be calculated using a similar formula as (2.9) except a minor change considering different load type, which is presented below.

$$F_b(a_b)=\left[\frac{3EA_b\pi^4}{16L_b^3}\left\{\left(a_{2sp}-a_b\right)^3-3h\left(a_{2sp}-a_b\right)^2+2h^2\left(a_{2sp}-a_b\right)\right\}+\frac{2\pi^4}{L_b^3}\left(a_{2sp}-a_b\right)EI_b\right]\cdot\frac{1}{\sin^2\left(\frac{\pi L_p}{L_b}\right)}, \tag{3.12}$$

where $a_b=d_b\dfrac{1}{\sin^2\left(\frac{\pi L_p}{L_b}\right)}$, and L_b, A_b, and I_b are length, cross-section area, and moment of inertia of the buckled beam, respectively. a_{2sp} is the amplitude of the second stable position and L_p is the distance of the pushing arm from the anchor.

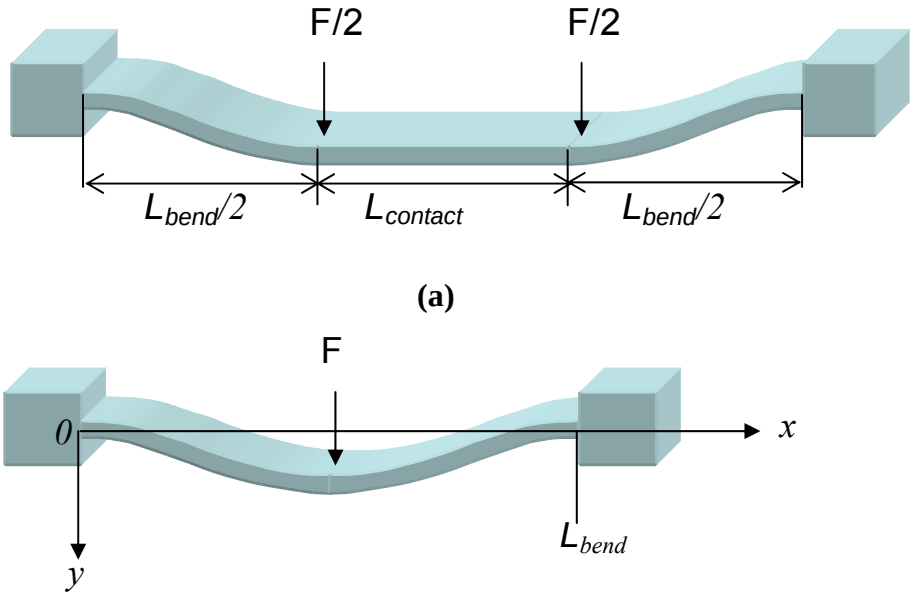

Figure 3.11. Sketch of (a) the ground, and (b) the simplified ground when being pushed.

By equalizing equations 3.11 and 3.12, one can find d_b and d_{GND} for given d_{OL}. What is more relevant to the switch design is to find minimum d_{OL} that can make the ground line touch the signal line, or that makes d_{GND} to be same as the gap between the signal line and the ground line. When gap = 10 μm, L_b = 2000 μm, h = 30 μm, and L_p = 500 μm, minimum required overlap d_{OL} is 10.34 μm and the restoring force of the ground line is 25.6 μN. Detailed calculation using the MathCAD software can be found in **Appendix**.

3.5 Process Design

Fabrication process flow of the proposed switch is illustrated in Fig. 3.12. The cross-sections correspond to *A-A'* line of Fig. 3.1. Except the parylene process, the fabrication flow is similar to that of the buckled-beam actuator, which is discussed in detail in the Chapter II. Having reasonable RF characteristics (loss tangent: 0.0037 at 1 MHz) and fast etch rate in HF, Borofloat glass was chosen as a substrate. To obtain high isolation, d, the gap between the signal line and the ground line at the "off" state, has to be as small as possible, which can be deduced from equations (3.8) and (3.9). For that purpose, to achieve straight sidewalls is very important, and hence, the SU-8 process and the parylene conformal coating process were selected.

3.6 Experiment result

Development of the fabrication process has been almost completed except the parylene process. RF characteristics should be measured with parylene on the sidewalls of the transmission lines. Isolation is closely related with surface roughness of the sidewalls of the signal and ground lines. Figure 3.13(b) and (c) show SEM images of

the sidewalls of a ground line and of a signal line, respectively. Insertion loss is expected to be very low, since the switch is minimally different from a conventional CPW.

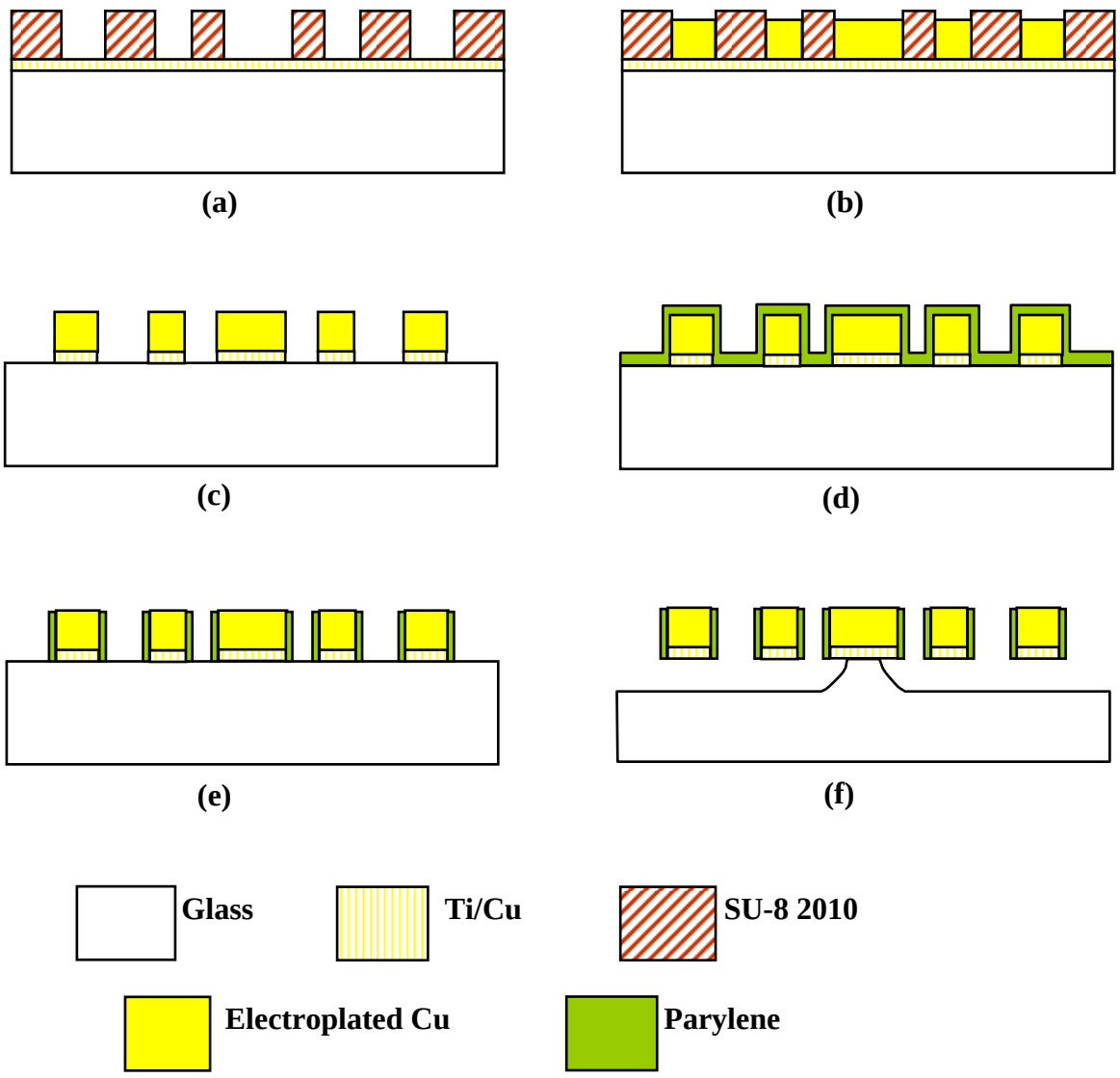

Figure 3.12. Fabrication process flow of the proposed switch: (a) seed metal deposition & SU-8 patterning, (b) Cu electroplating, (c) SU-8 removal, (d) parylene coating, (e) parylene anisotropic etching, and (f) glass substrate etching.

Mechanical operation of the switches has been observed under a microscope as shown in Fig. 3.14. Most of the buckled-beams did not remain at the second stable positions (Fig. 3.14(a)) after current is withdrawn, but bounced back to the original positions (Fig. 3.14(b)). The reason is considered to be that mild tensile stress of the electroplated copper reduces reverse critical load of buckled-beams, but increases the spring constants of the ground lines, resulting in higher ground line restoring force than reverse critical load, or $F_{crb} < F_{GND}$. Some buckled-beams with high initial rise (30 μm) remained near the second stable positions pushing the ground lines after current was withdrawn. However, due to larger spring constants of ground lines than designed, buckled beams failed to push ground lines enough for them to make contacts with signal lines, and left gaps between them, even though restoring force of ground lines was smaller than the reverse critical load (F_{crb}). This is the same situation as illustrated in Fig. 3.9(b): $F_b < F_{contact}$, $F_{GND} < F_{crb}$.

3.7 Summary and further works

In this thesis, a laterally driven RF MEMS switch has been designed, fabricated, and demonstrated up to mechanical operation. Simulation results utilizing the Sonnet Suit lite showed promising RF performances (isolations and insertion losses) of the switch. The fabrication process is cost effective, and post-CMOS-process compatible (low temperature process, < 100 °C). The process yield was as high as 90 percent.

The future work is to solve an issue of incomplete contact after current withdrawal. One promising method is to increase backward critical load. There are two ways to achieve this. First, an array of connected two or more buckled can be used as suggested

in the chapter II (Fig. 3.15(a)). Second, to increase initial rise (Fig. 3.15(b)) can provide similar effect. Increasing beam thickness is not a proper method as discussed in the chapter II; it results in severe secondary effects.

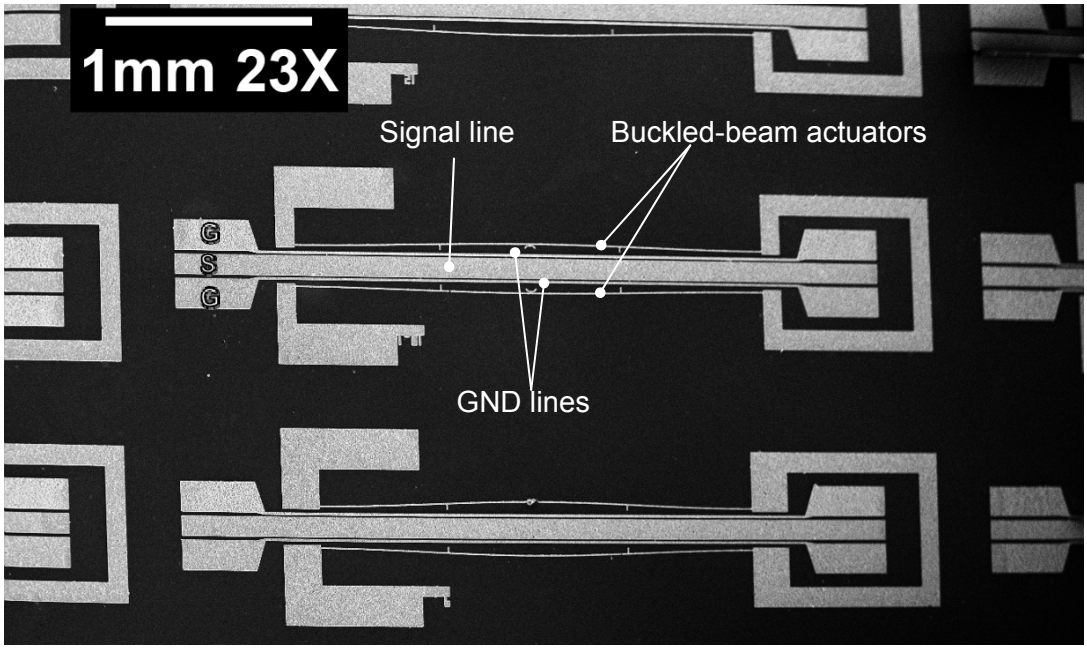

(a)

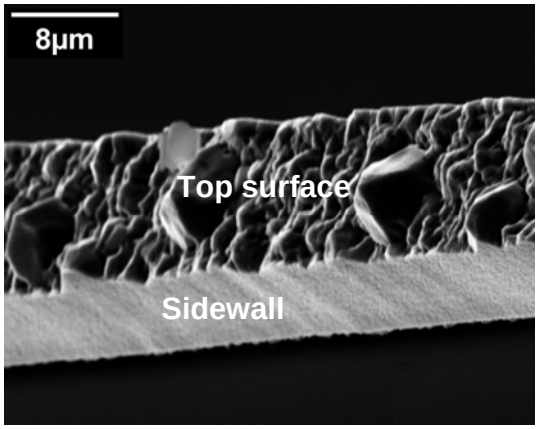

(b)

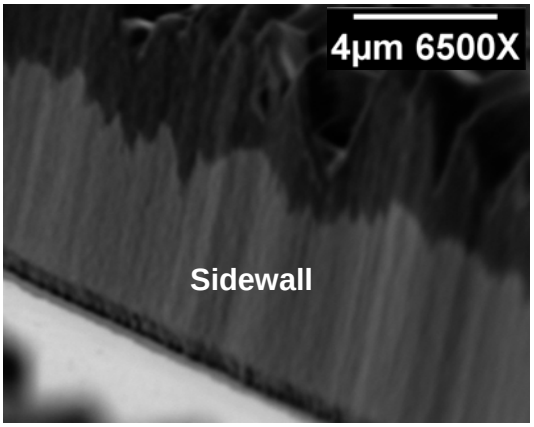

(c)

Figure 3.13. SEM micrographs of (a) the fabricated switches, (b) a ground line, and (c) a signal line.

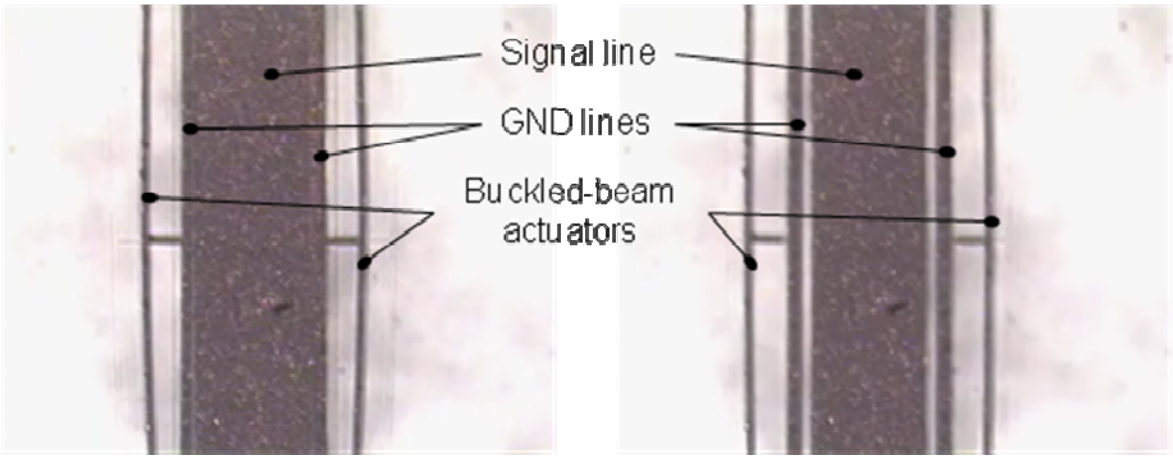

(a) **(b)**

Figure 3.14. Micrographs (a) when buckled-beams push ground lines (switch off-state), and (b) when buckled-beams are detached from ground lines (switch on-state).

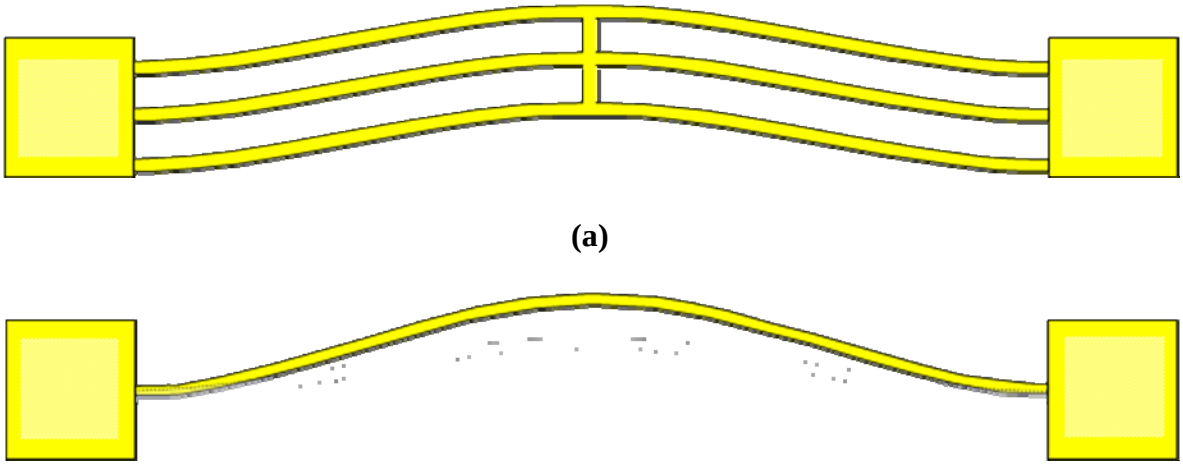

(a)

(b)

Figure 3.15. Sketches of (a) a buckled-beam array with connection in the middle, and (b) a buckled-beam with increased initial rise.

CHAPTER IV. CONCLUSION

A noble laterally driven RF MEMS switch with electromagnetic buckled-beam actuators has been proposed. At the on-state which is same as the as-fabricated state, the actuators are detached from the ground lines, and hence exert minimum influence on the coplanar waveguide (CPW) that is located in between the actuators. At this state, RF signal can flow unperturbed except a small loss. As currents flow through the actuators, the actuators move towards the ground lines by the Lorentz force and if the currents are high enough to move the actuators beyond the critical displacements, they push the ground lines to be contacted with the signal line, which is called as the "off-state" because now most of the RF signal is reflected due to this low impedance section that causes severe impedance mismatch. Due to bistability of the buckled-beams, the ground lines and the actuators do not return to their original positions when the currents are removed. To move the actuators back to their original positions and change the state of the switch from "off" to "on", reverse currents have to be applied to the actuators.

In this thesis, CPWs and buckled-beam actuators have been designed and fabricated on a borofloat glass wafer. The structures, i.e. CPWs and buckled-beams, are made of electroplated copper. Sustained structures were fabricated by under-etching the glass wafer with concentrated HF. All sidewalls of the structures will be covered with dielectric (parylene C) to prevent DC contacts between ground lines and signal lines, and between actuators and ground lines. The fabrication process flow is in an order of

seed layer deposition, SU-8 lithography, copper electroplating, SU-8 removal, seed layer strip, parylene coating, and release by substrate under-etch.

DC measurement has been carried out on buckled-beam actuators and proposed switches. The resistivity (ρ_{ec}) of electroplated copper was measured as 2×10^{-8} Ω m. Beams with various dimensions were actuated by current in a range of 10 to 200 mA which corresponds to a voltage range of 20 to 400 mV. Driving force ranged from 10 to 200 μN and the beam displacement was from 20 to 60 μm. Since the actuator consumes no power at each of the stable states, it is very useful in low power applications. Its low operation voltage makes it compatible with MMICs. Performance of the buckled-beam actuators outweigh other actuators with high force, low power consumption, fast actuation speed, low actuation voltage.

A buckled-beam actuator is a useful device for various applications including memory cells, micro-relays, micro-valves, optical switches, and digital micro-mirrors. It allows removal of actuation force during idle periods without affecting an actuated state of a device, which makes standing power consumption completely unnecessary. Simulation results utilizing the Sonnet Suit lite showed promising RF performances (isolations and insertion losses) of the switch. The fabrication process is cost effective, and post-CMOS-process compatible (low temperature process, < 100 °C). The process yield was as high as 90 percent. The proposed RF MEMS switch finds a variety of usefulness in RF circuits and systems, including wireless communication devices – antenna switching, T/R (transmitter/receiver) switching, band selection, adjustable gain

amplifiers; radar systems for military applications – phase shifters, phased array antennas; measurement equipments – impedance matching circuits, etc.

The future work is to solve an issue of incomplete contact between the signal line and ground lines after current withdrawal. One promising method is to increase backward critical load. There are two ways to achieve this: an array of connected two or more buckled beams, and increment of the initial rise.

Bibliography

[1.1] K.E. Peterson, "Micromechanical Membrane Switches on Silicon," *IBM J. Res. Develop.,* vol. 23, no. 4, pp. 376-385, July 1979.

[1.2] A. Gopinath and J. B. Rankin, “GaAs FET RF switches,” *IEEE Trans. Electron Devices* vol. 32, pp. 1272–8, 1985.

[1.3] R. H. Caverly, “Distortion in arsenide MESFET switches,” *IEEE Trans. Microwave Theor. Techni.,* vol. 41, pp. 1323–8, 1993.

[1.4] Y. Ota, M. Sakakura, K. Fujimoto, S. Yamamoto and H. Fujimoto, “High isolation and low insertion loss switch IC using GaAs MESFET’s,” *IEEE Trans. Microwave Theor. Technol.* vol. 43, pp. 2175–7, 1995.

[1.5] K. W. Kobayashi, A. K. Oki, D. K. Umemoto, S. K. Z. Claxton and D. C. Streit ,“Monolithic GaAs HBT p–i–n diode variable gain amplifiers, attenuators, and switches,” *IEEE Transactions on Microwave Theory and Techniques,* vol. 41, pp. 2295–302, 1993.

[1.6] G. M. Rebeiz, “RF MEMS – theory, design, and technology,” p. 5, John Wiley and Sons, 2003.

[1.7] J.J. Yao and M.F. Chang, "A Surface Micromachined Miniature Switch for Telecommunications Applications with Signal Frequencies f'rom DC up to 4 *GHz," Transducers '95,* pp. 384-387, 1995.

[1.8] C. Goldsmith, T.H. Lin, B. Powers, W.R. Wu, B. Norvell, "Micromechanical Membrane Switches for Microwave Applications," *IEEE Microwave Theory Tech. Symp.,* pp. 91-94, 1995.

[1.9] C. Goldsmith, T. H. Lin, B. Powers, R. W. Wen, and B. Norvell, “Micromechanical membrane switches for microwave applications,” in *IEEE Microwave Theory Tech. Symp.,* vol. 1, pp. 91–94, 1995.

[1.10] C. Goldsmith, J. Randall, S. Eshelman, T. H. Lin, D. Denniston, S. Chen, and B. Norvell, “Characteristics of micromachined switches at microwave frequencies,” *IEEE Microwave Theory Tech. Symp.* vol. 2, pp. 1141–1144, June 1996.

[1.11] Z. Jamie Yao, S. Chen, S. Eshelman, D. Denniston, and C. Goldsmith, "Micromachined Low-Loss Microwave Switches," *IEEE Journal of Microelectromechanical Systems*, vol. 8, no. 2, 1999.

[1.12] C. Goldsmith, Z. Yao, S. Eshelman, and D. Denniston, "Performance of Low-Loss RF MEMS Capacitive Switches," *IEEE Microwave and Guided Wave Letters*, vol. 8, no. 8, pp. 269-271, 1998.

[1.13] J. J. Yao and M. F. Chang, "A surface micromachined miniature switch for telecommunications applications with signal frequencies from DC up to 4 GHz," *Int. Conf. On Solid-State Sensors and Acutators Dig.*, Stockholm, Sweden, pp. 384–387, 1996.

[1.14] J. B. Muldavin and G. M. Rebeiz, "High Isolation CPW MEMS Shunt Switches Part 1: Modeling," *IEEE Transactions on Microwave Theory and Techniques*, pp. 1-8, 1999.

[1.15] Z. J. Yao, S. Chen, S. Eshelman, D. Denniston and C. Goldsmith, "Micromachined low-loss microwave switches," *IEEE Journal of Microelectromechanical Systems,* vol, 8 pp. 129–34, 1999.

[1.16] Z. Feng, W. Zhang, B. Su, K. F. Harsh, K.C. Gupta, V. Bright and Y.C. Lee, "Design and Modeling of RF MEMS Tunable Capacitors Using Electro-thermal Actuators," *IEEE MTT-S Digest*, pp. 1507-1510, 1999.

[1.17] J. B. Muldavin, G. M. Rebeiz, "30 *GHz* Tuned MEMS Switches", *IEEE MTT-S* Digest, pp. 1511-1514. 1999.

[1.18] M. Tang, A.Q. Liu, A. Agarwal, Q.X. Zhang and P. Win, "A New Approach of Lateral RF MEMS Switch," *Analog Integrated Circuits and Signal Processing*, vol. 40, pp. 165–173, 2004.

[1.19] M. Tang, A. Q. Liu, A. Agarwal, "A Compact DC - 20 GHz SPDT Switch Circuit Using Lateral RF MEMS Switches," *APMC2005 Proceedings*, 2005.

[1.20] J. H. Corntois, V. M. Bright, "Applications for surface-rnicromachined polysilicon thermal actuators and arrays," *Sensors and Actuators A,* vol. 58, pp. 19-25, 1997.

[1.21] Q. Huang and N. K. S. Lee, "Analysis and design of polysilicon thermal flexure actuator," *J. Micromech. Microeng.*, vol. 9, pp. 64–70, 1999.

[1.22] C. H. Ahn, Kim Y J and Allen M G, "A planar variable reluctance magnetic micromotor with fully integrated stator and coils," *J. Microelectromech. Syst.*vol. 2, pp. 165–73, 1993.

[1.23] J. S. Ko, M. L. Lee, D. S. Lee, C. A. Choi and Y. T. Kim, "Development and application of a laterally driven electromagnetic microactuator," *Appl. Phys. Lett*., vol. 81, pp. 547-549, 2002.

[1.24] L. K. Lagorce, O. Brand and M. G. Allen, "Magnetic microactuators based on polymer magnet," *J. Microelectromech. Syst.,* vol. 8, pp. 2–9, 1999.

[2.1] M. Hoffmann, P. Kopka, and E. Voges, "All-silicon bistable micromechanical fiber switch based on advanced bulk micromachining", IEEE Journal on Selected Topics in Quantum Electronics, Vol 5:1, 46–51, 1999.

[2.2] B. Jensen and L. G. Salmon, "Design of two-link, in-plane, bistable compliant micro-mechanisms", J Mech Design, vol. 121, no. 3, 416-423, 1999.

[2.3] X. Liu, J. Kubby, J. Chen, J. Diehl, K. Feinberg, K. German, P. Gulvin, L. Herko, N. Jia, P. Lin, J. Ma, J. Meyers, P. Nystrom, and Y. R. Wang., "Optical add and drop multiplexer using on-chip integration of planar light circuits and optical microelectromechanical system switching," *J. Vac. Sci. Tech. A*, vol. 22, no. 3, pp. 826-830, 2004.

[2.4] L. J. Hornbeck, T. R. Howell, R. L. Knipe, and M. A. Mignardi, "Digital micromirror device—Commercialization of massively parallel MEMS technology," *Proc. ASME Int. Mech. Eng. Congr. Expo.*, vol. DSC-62, HTD-354, pp. 3–8, 1997.

[2.5] J. Lee, M. Lee, W. Jang, C. Choi, and J. Joo, "Bi-stable planar polysilicon microactuators with shallow arch-shaped leaf springs," in *Proc. SPIE Conference on Micromachined Devices and Components V*, pp. 274-279, 1999.

[2.6] M. T. A. Saif, “On a tunable bistable MEMS-theory and experiment”, *J MEMS*, vol. 9:2, pp. 157 –170, 2000.

[2.7] J. Qiu, J. H. Lang, A. H. Slocum, “A curved-beam bistable mechanism, ” *J. MEMS*, vol. 13, no. 2, pp. 137-146, 2004.

[2.8] MicroChem Corp. http://microchem.com/products/su_eight.htm

[2.9] Omega Optical Inc. https://www.omegafilters.com

[2.10] K. R. Williams, K. Gupta, and M. Wasilik, “Etch Rates for Micromachining Processing—Part II,” *J. MEMS*, vol. 12, no. 6, pp. 761-778, 2003.

[2.11] K. P. Larsen, J. T. Ravnkilde, M. Ginnerup, O. Hansen, “Devices for fatigue testing of electroplated nickel (MEMS),” *J. MEMS,* vol. 12, pp. 443-446, 2002.

[2.12] V.A. Vas_ko, I. Tabakovic, S.C. Riemer, M.T. Kief, “Effect of organic additives on structure, resistivity, and room-temperature recrystallization of electrodeposited copper,” *Microelectronic Engineering*, vol. 75, pp. 71–77, 2004.

[2.13] S. H. Brongersma, E. Kerr, I. Vervoort, A. Saerens, K. Maex, “Grain growth, stress, and impurities in electroplated copper,” *J. Mater. Res.*, vol. 17, no. 3, 2002.

[2.14] A. Tarraf1, J. Daleiden, S. Irmer, D. Prasai and H. Hillmer, “Stress investigation of PECVD dielectric layers for advanced optical MEMS,” *J. Micromech. Microeng.*, vol. 14 pp. 317–323, 2004.

[2.15] F. Ericson, S. Greek, J. S¨oderkvist and J. Schweitz “High sensitivity surface micromachined structures for internal stress and stress gradient evaluation,” *J. Micromech. Microeng.* vol. 7, pp. 30–6, 1997.

[3.1] J. J. Yao, “RF MEMS from a device perspective,” *J. Micromech. Microeng.*, vol. 10, pp. R9-R38, 2000.

[3.2] C. Goldsmith, J. Ehmke, A. Malczewski, B. Pillans, S. Eshelman, Z. Yao, J. Brank, and M. Eberly, “Lifetime characterization of capacitive RF MEMS switches,” in *IEEE Int. Microwave Symp. Dig.*, pp. 227-230, 2001.

[3.3] Sonnet Software, Inc. http://www.sonnetsoftware.com/products/lite/

[3.4] CPW web calculator, http://www.eecircle.com/applets/015/Gcpw.html

APPENDIX

Detailed MathCAD calculation file.

BUCKLED-BEAM FORCE

$um := 10^{-6}$

$E := 128 \cdot 10^{9}$ Copper Young's modulus

$w := 10\ um$ Buckled-beam vertical dimension

$t := 5\ um$ Buckled-beam horizontal dimension

$l := 3000\ um$ Buckled-beam length

$l_{arm} := 30\ um$ Buckled-beam arm length

$h := 30\ um$ Buckled-beam initial rise

$h_{min} := 1.886 \cdot t$ Minimum buckled-beam initial rise for bistability

$$\frac{h_{min}}{um} = 9.43$$

$A_{bb} := w \cdot t$ Buckled-beam area

$I := \frac{w \cdot t^3}{12}$ Buckled-beam moment of inertia

Applied uniform load * length of buckled-beam

$$q(a_1) := \frac{3 \cdot E \cdot A_{bb} \cdot \pi^4}{8 \cdot l^3} \cdot \left(a_1^3 + 3 \cdot h \cdot a_1^2 + 2 \cdot h^2 \cdot a_1 \right) + \frac{4 \cdot \pi^4 \cdot a_1 \cdot E \cdot I}{l^3}$$

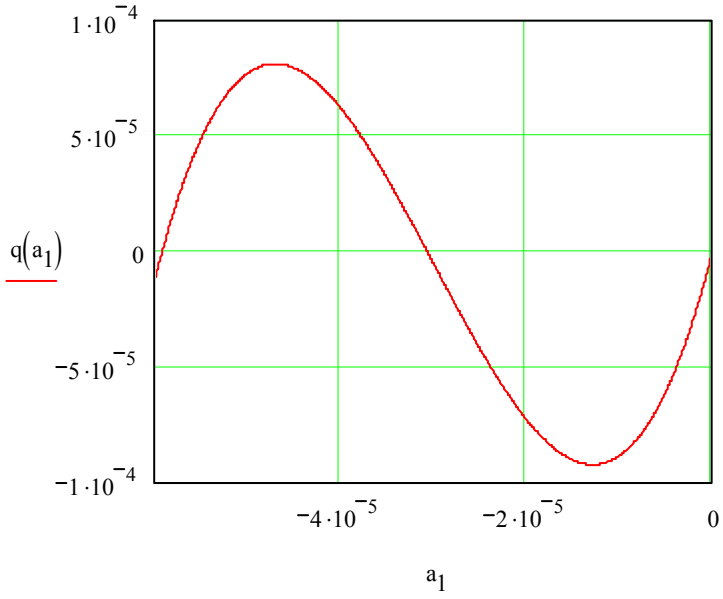

$$a_{crf} := -h + \sqrt{\frac{h^2}{3} - \frac{8 \cdot t^2}{27}}$$

Forward critical amplitude

$$a_{crf} = -1.289 \times 10^{-5}$$

$$a_{crb} := -h - \sqrt{\frac{h^2}{3} - \frac{8 \cdot t^2}{27}}$$

Reverse critical amplitude

$$a_{crb} = -4.711 \times 10^{-5}$$

$$q_{crf} := \frac{-\pi^4 \cdot E \cdot I \cdot t}{l^3} \cdot \left[9 \cdot \left(\frac{\alpha^2}{3} - \frac{8}{27} \right)^{1.5} + 4\alpha \right]$$

Forward critical force

$$q_{crf} = -9.244 \times 10^{-5}$$

$$q_{crb} := \frac{-\pi^4 \cdot E \cdot I \cdot t}{l^3} \cdot \left[-9 \cdot \left(\frac{\alpha^2}{3} - \frac{8}{27} \right)^{1.5} + 4\alpha \right]$$ Reverse critical force

$$q_{crb} = 8.09 \times 10^{-5}$$

$$a_{2sp} := -1.5 \cdot h - \frac{\sqrt{9 \cdot h^2 - 32 t^2}}{6}$$ The other bistable point

$$a_{2sp} = -5.924 \times 10^{-5}$$

$$q\left(a_{2sp}\right) = 0$$

RESTORING FORCE OF GROUND LINE

$L_{contact} := 1000\,um$ Length of the contact section

$L_{total} := 3000\,um$ Total length of the floating section

$$L_{bend} := \frac{L_{total} - L_{contact}}{2}$$ Length of one bending section

$w_{GND} := 10\,um$ Ground line vertical dimension

$t_{GND} := 10\,um$ Ground line horizontal dimension

$$I_{GND} := \frac{w_{GND} \cdot t_{GND}^3}{12}$$

$d_{GND} := 10\,um$ Desirable ground line displacement

$$F_{GND} := \frac{192 \cdot E \cdot I_{GND}}{\left(2L_{bend}\right)^3} \cdot d_{GND}$$

$F_{GND} = 2.56 \times 10^{-5}$ Resotoring force of ground line

Contact situation
P1 is the distance of pinpoint from the anchor

$$P_1 := \frac{l - L_{contact}}{2}$$

$$\frac{P_1}{um} = 1 \times 10^3$$

$$F_{crb} := \frac{\pi^4 \cdot E \cdot I \cdot t}{l^3} \cdot \left[\frac{9}{2} \cdot \left(\frac{\alpha^2}{3} - \frac{8}{27} \right)^{1.5} - 2\alpha \right] \cdot \frac{1}{\sin\left(\frac{\pi \cdot P_1}{l} \right)^2}$$ Backward critical force

$$F_{crb} = 5.393 \times 10^{-5}$$

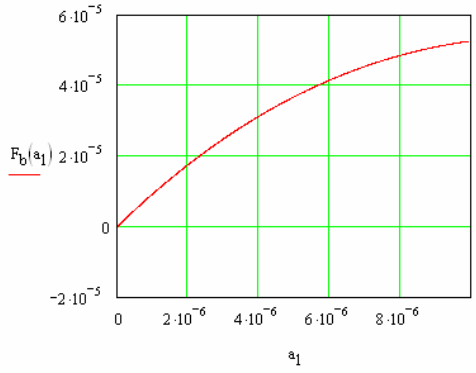

$$Disp_{cr\_rev} := a_{crb} - a_{2sp}$$

$$\frac{Disp_{cr\_rev}}{um} = 12.135$$ Reverse critical displacement in this new situation

ELECTROMAGNETIC FORCE

$B := 0.7$ Magnetic field (tesla)

$I_{crf} := \frac{-q_{crf}}{B \cdot l}$

Lorentz force = B*I*l_bb = ql_cr

$I_{crb} := \frac{-F_{crb}}{B \cdot l}$

$I_{crf} = 0.044$ Critical current for forward flip

$I_{crb} = -0.026$ Critical current for reverse flip

$\rho_{cu} := \frac{1}{5.8 \cdot 10^{7}}$ Copper resistivity

$R_{bb} := \rho_{cu} \cdot \frac{l}{A_{bb}}$ Resistance of the buckled-beam

$R_{bb} = 1.034$

$Act\_vol := R_{bb} \cdot I_{crf}$ Forward critical actuation voltage

$Act\_vol\_2 := R_{bb} \cdot I_{crb}$ Reverse critical actuation voltage

$Act\_vol = 0.046$

$Act\_vol\_2 = -0.027$

When there is an overlap between buckled-beam and the ground lines by d_OL F_b(d_b) = F_GND(d_OL-d_b)

$d_{OL1} := 10\ um$

guess

$d_{b1} := 3\ um$

Given

$$\frac{F_b(d_{b1})}{\frac{F_{GND}}{d_{GND}}(d_{OL1} - d_{b1})} = 1$$

$\frac{Find(d_{b1})}{um} = 2.292$ Equilibrium position of both, must be smaller than critical displacement, Disp_cr_rev

Let's find d_OL that will make the ground line displacement to become the set displacement

guess

$d_{b2} := 5\ um$

Given

$$\frac{F_b(d_{b2})}{F_{GND}} = 1$$

$d_b := Find(d_{b2})$

$\frac{d_b}{um} = 3.115$

$F_{GND} = 2.56 \times 10^{-5}$

$F_b(d_b) = 2.56 \times 10^{-5}$

$$xx_2 := Disp_{cr\_rev} - d_b$$

$$xx_2 = 9.019 \times 10^{-6}$$

The distance between the rev. critical pt. & the pt. beam dsp. force=GND restoring force

$$xx_{1\_P1} := d_b \cdot \sin\left(\frac{\pi \cdot P_1}{l}\right)^2$$

$$xx_{2\_P1} := xx_2 \cdot \sin\left(\frac{\pi \cdot P_1}{l}\right)^2$$

$$xx_{2\_P1} = 6.765 \times 10^{-6}$$

The distance between buckled-beam anchor and ground line (Distance)

$$a_{b2\_P1} := \sin\left(\frac{\pi \cdot P_1}{l}\right)^2 \cdot a_{2sp}$$

$$a_{b2\_P1} = -4.443 \times 10^{-5}$$

Buckled_beam movement range at P1

$$h_{P1} := h \cdot \sin\left(\frac{\pi \cdot P_1}{l}\right)^2$$

Buckled_beam initial rise at P1

$$Distance := \left(-a_{b2\_P1} - h_{P1} + l_{arm} - xx_{1\_P1} - d_{OL} - \frac{xx_{2\_P1}}{2}\right)$$

$$\frac{Distance}{um} = 33.096$$

Required current and voltage

$I_{crf} = 0.044$

$crr1(x) := \frac{d}{dx} q(x)$

$Act\_vol = 0.046$

guess

$x1 := -30\,um$

Given

$crr1(x1) = 0$

$xxx1 := Find(x1)$

$xxx1 = -1.289 \times 10^{-5}$

ISOLATION BY CONTACT AREA

$\varepsilon_r := 2.6$ Relative permittivity of Parylene

$\varepsilon_p := 8.85 \cdot 10^{-12}$ Permittivity in air

$t_{GND} := 10\,um$ Ground thickness

$d_{prl} := 0.2 \cdot um$ Distance betw. GND and Sign. Lines at off-state

$f_1 := 20 \cdot 10^9$ $f_2 := 40 \cdot 10^9$ Frequencies

$\omega_1 := 2 \cdot \pi \cdot f_1$ $\omega_2 := 2 \cdot \pi \cdot f_2$ Angular frequencies

$i := \sqrt{-1}$

$Z_0 := 50$ Characteristic impedance

$$C_d(l_{contact}) := 2\varepsilon_p \cdot \varepsilon_r \cdot \frac{t_{GND} \cdot l_{contact}}{d_{prl}}$$ Off state capacitance

$$S_{21\_f1}(l_{contact}) := \frac{1}{1 + i \cdot \omega_1 \cdot C_d(l_{contact}) \cdot \frac{Z_0}{2}}$$

$$S_{21\_f2}(l_{contact}) := \frac{1}{1 + i \cdot \omega_2 \cdot C_d(l_{contact}) \cdot \frac{Z_0}{2}}$$

$$Isolation_1(l_{contact}) := 10 \cdot \log\left[\left(\left|S_{21\_f1}(l_{contact})\right|\right)^2\right]$$ Isolations @20GHz

$$Isolation_2(l_{contact}) := 10 \cdot \log\left[\left(\left|S_{21\_f2}(l_{contact})\right|\right)^2\right]$$ Isolations @40Ghz

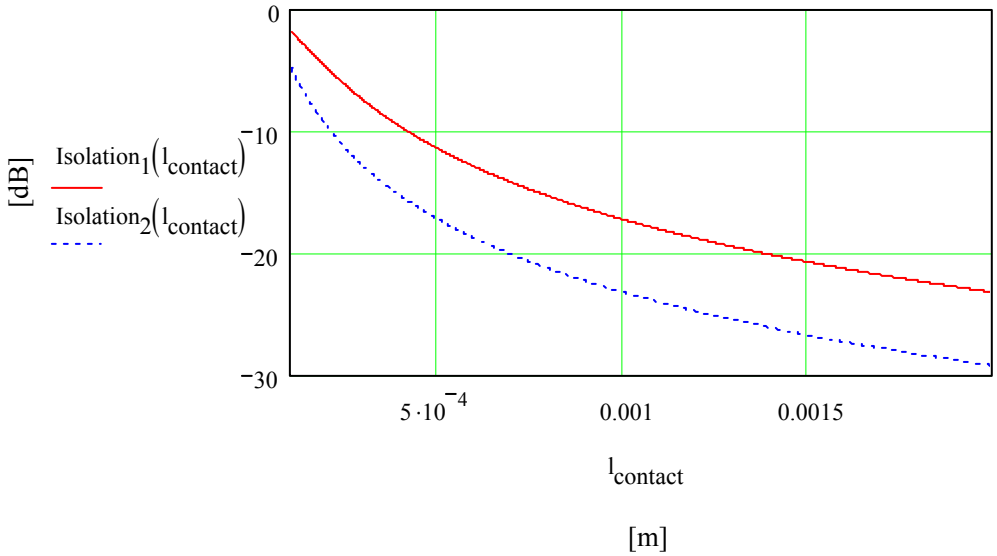

$\text{Isolation}_1(L_{contact}) = -17.264$ Isolation at 20GHz

$\text{Isolation}_2(L_{contact}) = -23.223$ Isolation at 40GHz

VITA

Seunghoon Park was born in Kangwon province on South Korea in December 11, 1979. He obtained his Bachelor of Science in Electronics Engineering from Dong-A University, Busan, South Korea in February 2005. He is expecting his Master of Science in Electrical & Computer Engineering from Louisiana State University, Baton Rouge, LA in December, 2007. His master's research area is RF MEMS and micro actuators.